MONKES: a fast neoclassical code for the evaluation of monoenergetic transport coefficients

F.J. Escoto[1]**, J.L. Velasco**[1]**, I. Calvo**[1]**, M. Landreman**[2] **and F.I. Parra**[3]

[1]Centro de Investigaciones Energéticas, Medioambientales y Tecnológicas.
Avenida Complutense 40, Madrid (Madrid) 28040
[2]University of Maryland, College Park, MD, USA
[3]Princeton Plasma Physics Laboratory, Princeton, NJ 08540, USA

E-mail: `fjavier.escoto@ciemat.es`

April 2023

Abstract. `MONKES` is a new three dimensional neoclassical code to evaluate monoenergetic transport coefficients in large aspect ratio stellarators. Apart from traditional neoclassical studies, `MONKES` can be used to target these coefficients in a stellarator optimization process. The code is spectral in the three variables, and uses a block tridiagonal algorithm for solving the resultant linear system of equations. These two features allow to compute, in a single processor, monoenergetic coefficients sufficiently fast to be included in an optimization suite.

1. Introduction

Stellarators are three-dimensional magnetic confinement devices which are promising candidates for a fusion reaction power plant. In order to achieve magnetic confinement of fusion plasmas, Poincaré-Hopf theorem requires that (to have non-vanishing magnetic fields), the field lines must be tangent to a topologically toroidal surface called flux surface [1]. In addition, magnetic field lines must have the so called rotational transform, which means that, when following a magnetic field line, the line rotates both in the toroidal and poloidal directions. For stellarators, such magnetic field can be created entirely by external magnets. In contrast, tokamaks rely on the current driven by the plasma to generate rotational transform, which makes them intrinsically non-steady and more sensitive to magnetohydrodynamic instabilities. Thus, stellarators are potentially an attractive alternative to the tokamak concept for a fusion power plant. However, tokamaks posses a property which stellarators lack: axisymmetry. This additional symmetry implies, as a consequence of Noether's theorem, that collisionless orbits of all charged particles in the magnetic field experience a zero secular radial drift. That is, when their movement is averaged, they remain in the same flux surface in which they were born and therefore are well confined. In a tokamak, the main neoclassical mechanism of particle loss is due to collisions, which alter their otherwise confined trajectories. On the other hand, in a stellarator, magnetic geometry interplays with collisions enhancing radial neoclassical transport. Hence, stellarator magnetic fields must be neoclassically optimized to improve their confinement properties. The most general class of stellarators which shares the tokamak property of zero secular radial drift is the omnigenous stellarator. Two different subclasses of omnigenous stellarator have drawn much attention in the past and recent years: quasi-symmetric (QS) and quasi-isodynamic (QI) stellarators. Examples of the former subclass are the Helically Symmetric eXperiment (HSX) or the unfinished National Compact Stellarator Experiment (NCSX). The neoclassical properties of QS stellarators are isomorphic to those in an equivalent tokamak [2], [3], and by means of stellarator optimization it is possible to design magnetic fields with extremely low neoclassical losses [4]. Of the latter subclass, the Wendelstein 7-X (W7-X) experiment was conceived to be close to QI and demonstrates [5] that theoretically based stellarator optimization can be applied to construct a device with much better confinement properties than any of the previously built three-dimensional machines. Quasi isodynamic configurations have the additional property (besides omnigeneity) that contour lines of constant magnetic field strength in a flux surface close poloidally.

This constraint has an important implication: QI stellarators produce zero bootstrap current to first order in a low collisionality expansion [6], [7]. Bootstrap current makes the magnetic configuration sensitive to plasma pressure and its effect should be taken into account to ensure that the stellarator good confinement is robust throughout all of its modes of operation. For instance, for stellarators with an island divertor, it can bring the chain of islands to inner radial positions [8]. Hence, from the non symmetric omnigenous configurations, the QI concept has drawn most of the attention and enormous effort has been put in obtaining stellarators sufficiently close to QI [9], [cite JL robust optimization paper], [10], [11], [12]. Other non-QI omnigenous configurations have recently been investigated [13] and it remains unclear whether magnetic fields of this category can be as robust to plasma pressure effects as QI ones.

In order to improve the neoclassical confinement properties of stellarators, the straightforward approach is to include the relevant quantities to be minimized as targets in optimization suites. Ideally, one would obtain these targets by solving the most general drift-kinetic equation possible, which is five dimensional. However, solving such equation is not an easy task and in general takes too much time to be numerically solved, making this approach not feasible in practice. Neoclassical properties are typically addressed indirectly or by solving simplified versions of the drift-kinetic equation. The latter approach has been successfully applied to produce quick calculations of radial fluxes of energy and particles. We give two examples of this success. Based on the rigorous derivations for low collisionality of [14] and [15] for almost omnigenous and large aspect ratio stellarators respectively, two bounce averaged drift-kinetic equations are solved very fast by the code KNOSOS [16], [17]. For the $1/\nu$ regime, the code NEO [18] computes the effective ripple ϵ_{eff}, which is a figure of merit for radial transport. Both of these codes are included in the stellarator optimization suite STELLOPT [19]. In what regards to parallel transport, the long mean free path formulas for flow and bootstrap current such as the ones given in [20], [21] or [22] have been used in the optimization process that lead to W7-X. However, although they can be computed very fast and might capture some qualitative behaviour, these formulae are plagued with noise due to resonances in rational surfaces and even with smoothing ad hoc techniques, they are not accurate [23]. Therefore, an accurate calculation of the bootstrap current is required to understand precisely how it is affected by other parameters of the magnetic field for optimization purposes. With the solely exception of precisely QS stellarators [23] (for which analytical formulae for

tokamaks are applicable), accurate calculations of the bootstrap current could not be calculated sufficiently fast and have been excluded of the optimization process in the past.

In this work we present MONKES (MONoenergetic Kinetic Equation Solver), a new neoclassical code conceived to satisfy the necessity of taking into account the bootstrap current effect in stellarator optimization suites. Specifically, MONKES makes possible to use as target monoenergetic geometric coefficient $\widehat{D}_{31}$ (its precise definition is given in section 2), which is related to the bootstrap current. This coefficient has a role of the driving force for the spontaneous parallel particle and heat flows in a neoclassical theory which uses a model momentum conserving collision operator [24]. Nevertheless, the code can be used not only for optimization purposes but as a replacement for the standard and successful neoclassical code DKES [25]. The paper is organized as follows: In section 2 the drift-kinetic equation that MONKES solves and the transport coefficients that computes. In section 3 the algorithm to solve the drift-kinetic equation and its implementation are described. In section 4 we demonstrate that MONKES can be used to compute accurate monoenergetic coefficients at low collisionality in less than 2 minutes in a single processor for the $1/\nu$ and $\sqrt{\nu}$ regimes. These computations are also benchmarked against DKES and when necessary with the code SFINCS [26]. Finally, in section 5 we summarize the results and comment future lines of work and applications for MONKES.

2. Drift-kinetic equation and transport coefficients

The new code MONKES solves the drift-kinetic equation presented in [27], which is solved by the standard neoclassical code DKES [25]. This equation reads

$$(v\xi\boldsymbol{b} + \boldsymbol{v}_E) \cdot \nabla h_a + v\nabla \cdot \boldsymbol{b}\frac{(1-\xi^2)}{2}\frac{\partial h_a}{\partial \xi} - \nu^a \mathcal{L}h_a$$
$$= S_a, \quad (1)$$

where we have employed as velocity coordinates the cosine of the pitch-angle $\xi := \boldsymbol{v} \cdot \boldsymbol{b}/|\boldsymbol{v}|$ and the module of the velocity $v := |\boldsymbol{v}|$, being $\boldsymbol{B}$ the magnetic field, $B := |\boldsymbol{B}|$ its strength and $\boldsymbol{b} = \boldsymbol{B}/B$ its unitary vector. For the spatial domain we use a system of coordinates in which flux surfaces are assumed to exist and are labelled by $\psi \in [0, \psi_{\text{lcfs}}]$ where ψ_{lcfs} denotes the label of the last closed flux surface. The solution to equation (1), h_a, is the deviation of the distribution function from a local Maxwellian

$$f_{Ma}(\psi, v) = n_a(\psi)\pi^{-3/2}v_{ta}^{-3}(\psi)\exp\left(-\frac{v^2}{v_{ta}^2(\psi)}\right), \quad (2)$$

for the plasma species a of charge e_a, mass m_a, density n_a and temperature $T_a(\psi)$ (in energy units), where $v_{ta} = \sqrt{2T_a/m_a}$ is its thermal velocity. For the convective term in equation (1)

$$\boldsymbol{v}_E := \frac{\boldsymbol{E}_0 \times \boldsymbol{B}}{\langle B^2 \rangle} = -E_\psi(\psi)\frac{\boldsymbol{B} \times \nabla\psi}{\langle B^2 \rangle} \quad (3)$$

denotes the incompressible $\boldsymbol{E} \times \boldsymbol{B}$ drift approximation and $\boldsymbol{E}_0 = E_\psi(\psi)\nabla\psi$ is the piece of the electric field perpendicular to the flux surface. The symbol $\langle ... \rangle$ stands for the flux surface average operation. We denote the Lorentz pitch-angle scattering operator by

$$\mathcal{L} = \frac{1}{2}\frac{\partial}{\partial \xi}\left((1-\xi^2)\frac{\partial}{\partial \xi}\right). \quad (4)$$

In the collision operator, $\nu^a(v) = \sum_b \nu^{ab}(v)$ and

$$\nu^{ab}(v) := \frac{4\pi n_b e_a^2 e_b^2}{m_a^2 v_{ta}^3}\log\Lambda\frac{\text{erf}(v/v_{tb}) - G(v/v_{tb})}{v^3/v_{ta}^3}, \quad (5)$$

stands for the pitch-angle collision frequency between species a and b. We denote the Chandrasekhar function by $G(x) = \left[\text{erf}(x) - (2x/\sqrt{\pi})\exp(-x^2)\right]/(2x^2)$ and $\log\Lambda$ is the Coulomb logarithm.

The solution of equation (1) is determined up to an additive function $g(\psi, v)$ which spans the nullspace of the drift-kinetic equation. This function is unimportant as it does not contribute to the transport coefficients, nevertheless, in order to have a unique solution to the drift-kinetic equation, it must be fixed by imposing an appropriate additional constraint. We will select this free function (for fixed (ψ, v)) by imposing

$$\left\langle \int_{-1}^{1} h_a \, \mathrm{d}\xi \right\rangle = C, \quad (6)$$

for some $C \in \mathbb{R}$ which will be determined indirectly.

In the right-hand-side of equation (1)

$$S_a := -\boldsymbol{v}_{\text{ma}} \cdot \nabla\psi\left(A_{1a} + \frac{v^2}{v_{ta}^2}A_{2a}\right)f_{Ma} - Bv\xi A_{3a}f_{Ma} \quad (7)$$

is the source term,

$$\boldsymbol{v}_{\text{ma}} \cdot \nabla\psi = -\frac{Bv^2}{\Omega_a}\frac{1+\xi^2}{2B^3}\boldsymbol{B} \times \nabla\psi \cdot \nabla B, \quad (8)$$

is the expression of the magnetic radial drift assuming ideal magnetohydrodynamical equilibrium, $\Omega_a = e_a B/m_a$ is the gyrofrecuency, the flux functions

$$A_{1a}(\psi) := \frac{\mathrm{d}\ln n_a}{\mathrm{d}\psi} - \frac{3}{2}\frac{\mathrm{d}\ln T_a}{\mathrm{d}\psi} - \frac{e_a E_\psi}{T_a}, \quad (9)$$

$$A_{2a}(\psi) := \frac{\mathrm{d}\ln T_a}{\mathrm{d}\psi}, \quad (10)$$

$$A_{3a}(\psi) := -\frac{e_a}{T_a}\frac{\langle \boldsymbol{E} \cdot \boldsymbol{B} \rangle}{\langle B^2 \rangle}, \quad (11)$$

are the so called thermodinamical forces.

Once the equation is solved, taking the moments $\{\boldsymbol{v}_{\mathrm{ma}} \cdot \nabla\psi, (v^2/v_{\mathrm{t}a}^2)\boldsymbol{v}_{\mathrm{ma}} \cdot \nabla\psi, v\xi B\}$ of h_a and then the flux-surface average yields respectively the radial particle and heat fluxes and the parallel flow

$$\langle \boldsymbol{\Gamma}_a \cdot \nabla\psi \rangle := \left\langle \int \boldsymbol{v}_{\mathrm{ma}} \cdot \nabla\psi \; h_a \, \mathrm{d}^3\boldsymbol{v} \right\rangle, \qquad (12)$$

$$\left\langle \frac{\boldsymbol{Q}_a \cdot \nabla\psi}{T_a} \right\rangle := \left\langle \int \frac{v^2}{v_{\mathrm{t}a}^2} \boldsymbol{v}_{\mathrm{ma}} \cdot \nabla\psi \; h_a \, \mathrm{d}^3\boldsymbol{v} \right\rangle, \qquad (13)$$

$$\langle n_a \boldsymbol{V}_a \cdot \boldsymbol{B} \rangle := \left\langle B \int v\xi \; h_a \, \mathrm{d}^3\boldsymbol{v} \right\rangle. \qquad (14)$$

It is a common practice for linear drift-kinetic equations (e.g. [27], [28], [26]) to apply superposition and split h_a in three additive terms. Each one of them is a solution to the drift-kinetic equation using as source one of the three summands of the right hand side of definition (7). Besides, as in the drift-kinetic equation (1) there are no derivatives or integrals along ψ nor v, it is convenient to use the splitting

$$h_a = f_{\mathrm{M}a} \left[\frac{Bv}{\Omega_a} \left(A_{1a} f_1 + A_{2a} \frac{v^2}{v_{\mathrm{t}a}^2} f_2 \right) + A_{3a} f_3 \right], \; (15)$$

relating h_a to three functions $\{f_j\}_{j=1}^3$, properly normalized so that they are solutions of

$$\xi \boldsymbol{b} \cdot \nabla f_j + \nabla \cdot \boldsymbol{b} \frac{(1-\xi^2)}{2} \frac{\partial f_j}{\partial \xi} - \frac{\hat{E}_\psi}{\langle B^2 \rangle} \boldsymbol{B} \times \nabla\psi \cdot \nabla f_j$$
$$- \hat{\nu} \mathcal{L} f_j = s_j, \qquad (16)$$

for $j = 1, 2, 3$, where $\hat{\nu} := \nu(v)/v$ and $\hat{E}_\psi := E_\psi/v$. The source terms are defined as

$$s_1 := -\boldsymbol{v}_{\mathrm{ma}} \cdot \nabla\psi \frac{\Omega_a}{Bv^2}, \quad s_2 := s_1, \quad s_3 := -\xi B. \; (17)$$

The relation between h_a and f_j given by equation (15) is such that the transport quantities (12), (13) and (14) can be written in terms of three transport coefficients which for fixed $(\hat{\nu}, \hat{E}_\psi)$ depend only on the magnetic configuration. As $\mathrm{d}\hat{\nu}/\mathrm{d}v$ never annuls, the dependence of f_j on the velocity v can be parametrized by its dependence on $\hat{\nu}$. Thus, for fixed $(\hat{\nu}, \hat{E}_\psi)$, equation (16) is completely determined by the magnetic configuration. Hence, its unique solutions f_j that satisfy a condition analogous to (6) are also completely determined by the magnetic configuration. The series of assumptions that lead to ψ and v appearing as mere parameters in the drift-kinetic equation (1) comprise the so called monoenergetic approximation to neoclassical transport (see e.g. [29]).

Using (15) we can write the transport quantities

(12), (13) and (14) in terms of the Onsager matrix

$$\begin{bmatrix} \langle \boldsymbol{\Gamma}_a \cdot \nabla\psi \rangle \\ \left\langle \dfrac{\boldsymbol{Q}_a \cdot \nabla\psi}{T_a} \right\rangle \\ \langle n_a \boldsymbol{V}_a \cdot \boldsymbol{B} \rangle \end{bmatrix} = \begin{bmatrix} L_{11a} & L_{12a} & L_{13a} \\ L_{21a} & L_{22a} & L_{23a} \\ L_{31a} & L_{32a} & L_{33a} \end{bmatrix} \begin{bmatrix} A_{1a} \\ A_{2a} \\ A_{3a} \end{bmatrix}.$$
$$(18)$$

We have defined the thermal transport coefficients as

$$L_{ija} := \int_0^\infty 2\pi v^2 f_{\mathrm{M}a} w_i w_j D_{ija} \, \mathrm{d}v, \qquad (19)$$

where $w_1 = w_3 = 1$, $w_2 = v^2/v_{\mathrm{t}a}^2$ and we have used that $\int g \, \mathrm{d}^3\boldsymbol{v} = 2\pi \int_0^\infty \int_{-1}^1 g v^2 \, \mathrm{d}\xi \, \mathrm{d}v$ for any integrable gyroaveraged function g. The quantities D_{ija} are the monoenergetic transport coefficients, defined as

$$D_{ija} := \frac{B^2 v^3}{\Omega_a^2} \widehat{D}_{ij}, \qquad i,j \in \{1,2\}, \qquad (20)$$

$$D_{i3a} := \frac{B v^2}{\Omega_a} \widehat{D}_{i3}, \qquad i \in \{1,2\}, \qquad (21)$$

$$D_{3ja} := \frac{B v^2}{\Omega_a} \widehat{D}_{3j}, \qquad j \in \{1,2\}, \qquad (22)$$

$$D_{33a} := v \widehat{D}_{33}, \qquad (23)$$

and $\widehat{D}_{ij}$ are the monoenergetic geometric coefficients. Namely,

$$\widehat{D}_{ij}(\psi, v) := \left\langle \int_{-1}^1 s_i f_j \, \mathrm{d}\xi \right\rangle, \quad i,j \in \{1,2,3\}. \quad (24)$$

Note that, unlike D_{ija}, the monoenergetic geometric coefficients $\widehat{D}_{ij}$ do not depend on the species for fixed $\hat{\nu}$ (however the correspondent value of v associated to each $\hat{\nu}$ varies between species) and depend only on the magnetic geometry. Of the monoenergetic geometric coefficients $\widehat{D}_{ij}$ only three of them are independent as Onsager symmetry implies $\widehat{D}_{13} = -\widehat{D}_{31}$. Hence, to obtain the transport coefficients for all species, requires to solve (16) for two different source terms s_1 and s_3. The algorithm for solving equation (16) is described in the next section.

3. Numerical method

In this section we describe the algorithm implemented to numerically solve the drift-kinetic equation (16). We drop the subscript j from that labels every different source term. Also, as ψ and v act as mere parameters we will omit their dependence in this section and functions of these two variables will be referred as constants. First, in subsection 3.1 we will present the algorithm in a formal and abstract manner which is valid for any set of spatial coordinates. The algorithm,

based on the tridiagonal representation of the drift-kinetic equation, merges naturally when discretizing the velocity coordinate ξ using a Legendre spectral method. Nevertheless, for convenience, we will explain it in (right-handed) Boozer coordinates $(\psi, \theta, \zeta) \in [0, \psi_{\text{lcfs}}] \times [0, 2\pi) \times [0, 2\pi/N_p)$. In these coordinates $2\pi\psi$ is the toroidal flux of the magnetic field and θ, ζ are respectively the poloidal and toroidal (in a single period) angles. The integer $N_p \geq 1$ denotes the number of periods of the device. In Boozer coordinates the magnetic field can be written as

$$
\begin{aligned}
\boldsymbol{B} &= \nabla\psi \times \nabla\theta - \iota(\psi)\nabla\psi \times \nabla\zeta \\
&= B_\psi(\psi, \theta, \zeta)\nabla\psi + B_\theta(\psi)\nabla\theta + B_\zeta(\psi)\nabla\zeta, \quad (25)
\end{aligned}
$$

and the Jacobian of the transformation reads

$$
\sqrt{g}(\psi, \theta, \zeta) := (\nabla\psi \times \nabla\theta \cdot \nabla\zeta)^{-1} = \frac{B_\zeta + \iota B_\theta}{B^2}, \quad (26)
$$

where $\iota := \boldsymbol{B} \cdot \nabla\theta / \boldsymbol{B} \cdot \nabla\zeta$ is the rotational transform. Using (25) and (26), the spatial differential operators present in the drift-kinetic equation (16) can be expressed in these coordinates as

$$
\boldsymbol{b} \cdot \nabla = \frac{B}{B_\zeta + \iota B_\theta}\left(\iota\frac{\partial}{\partial\theta} + \frac{\partial}{\partial\zeta}\right), \quad (27)
$$

$$
\boldsymbol{B} \times \nabla\psi \cdot \nabla = \frac{B^2}{B_\zeta + \iota B_\theta}\left(B_\zeta\frac{\partial}{\partial\theta} - B_\theta\frac{\partial}{\partial\zeta}\right). \quad (28)
$$

After the abstract explanation of the algorithm, in subsection 3.2 we explain how is implemented in `MONKES`.

3.1. Legendre polynomial expansion

The algorithm is based on the approximate representation of the distribution function f in a truncated Legendre series. We will search for approximate solutions to equation (16) of the form

$$
f(\theta, \zeta, \xi) = \sum_{k=0}^{N_\xi} f^{(k)}(\theta, \zeta)P_k(\xi), \quad (29)
$$

where $f^{(k)} = \langle f, P_k\rangle_{\mathcal{L}} / \langle P_k, P_k\rangle_{\mathcal{L}}$ is the $k-$th Legendre mode of $f(\theta, \zeta, \xi)$ (see Appendix A) and N_ξ is an integer greater or equal to 1. Of course, in general, the exact solution to equation (16) does not have a finite Legendre spectrum, but taking N_ξ sufficiently high in expansion (29) yields an approximate solution to the desired degree of accuracy (in infinite precision arithmetic).

In Appendix A we derive explicitly the projection of each term of the drift-kinetic equation (16) onto the Legendre basis when the representation (29) is used. When doing so, we get that the Legendre

modes of the drift-kinetic equation have the tridiagonal representation

$$
L_k f^{(k-1)} + D_k f^{(k)} + U_k f^{(k+1)} = s^{(k)}, \quad (30)
$$

for $k = 0, 1, \ldots, N_\xi$, where we have defined for convenience $f^{(-1)} := 0$ and from expansion (29) is clear that $f^{(N_\xi+1)} = 0$. Analogously to (29) the source term is expanded as $s = \sum_{k=0}^{N_\xi} s^{(k)}P_k$, and for the sources (17) the expansion is exact when $N_\xi \geq 2$. The spatial differential operators read

$$
L_k = \frac{k}{2k-1}\left(\boldsymbol{b} \cdot \nabla + \frac{k-1}{2}\boldsymbol{b} \cdot \nabla \ln B\right), \quad (31)
$$

$$
D_k = -\frac{\hat{E}_\psi}{\langle B^2\rangle}\boldsymbol{B} \times \nabla\psi \cdot \nabla + \frac{k(k+1)}{2}\hat{\nu}, \quad (32)
$$

$$
U_k = \frac{k+1}{2k+3}\left(\boldsymbol{b} \cdot \nabla - \frac{k+2}{2}\boldsymbol{b} \cdot \nabla \ln B\right). \quad (33)
$$

Thanks to its tridiagonal structure, the system of equations (30) can be formally inverted using the standard Gaussian elimination algorithm for block tridiagonal matrices. Before introducing the algorithm we will explain how to fix the free constant of the solution to equation (30) so that it can be inverted. Note that the aforementioned nullspace of the drift-kinetic equation translates in the fact that $f^{(0)}$ is not completely determined from equation (30). To prove this, we inspect the modes $k = 0$ and $k = 1$ that involve $f^{(0)}$. From expression (28) we can deduce that the term $D_0 f^{(0)} + U_0 f^{(1)}$ is invariant if we add to $f^{(0)}$ any function of $B_\theta(\psi)\zeta + B_\zeta(\psi)\theta$ when $\hat{E}_\psi \neq 0$ and does not include $f^{(0)}$ for $\hat{E}_\psi = 0$. Besides, the term $L_1 f^{(0)} + D_1 f^{(1)} + U_1 f^{(2)}$ remains invariant if we add to $f^{(0)}$ any constant. Thus, equation (30) is unaltered when we add to $f^{(0)}$ a constant. A constraint equivalent to condition (6) is to fix the value of the $0-$th Legendre mode of the distribution function at a single point of the flux-surface. For example,

$$
f^{(0)}(0, 0) = 0. \quad (34)
$$

With this condition, equation (30) has a unique solution and can be inverted (further details on its invertibility are given in Appendix B) to obtain an approximation of the first $N_\xi + 1$ Legendre modes of the solution to the drift-kinetic equation (16).

The algorithm for formally solving the truncated drift-kinetic equation (30) consists of two steps.

(i) **Forward elimination**

Starting from $\Delta_{N_\xi} = D_{N_\xi}$ and $\sigma^{(N_\xi)} = s^{(N_\xi)}$ we can obtain recursively the operators

$$
\Delta_k = D_k - U_k\Delta_{k+1}^{-1}L_{k+1}, \quad (35)
$$

and the sources

$$\sigma^{(k)} = s^{(k)} - U_k \Delta_{k+1}^{-1} \sigma^{(k+1)}, \qquad (36)$$

for $k = N_\xi - 1, N_\xi - 2, \dots, 0$ (in this order). Equations (35) and (36) define the forward elimination. With this procedure we can transform equation (30) to the equivalent system

$$L_k f^{(k-1)} + \Delta_k f^{(k)} = \sigma^{(k)}, \qquad (37)$$

for $k = 0, 1, \dots, N_\xi$. Note that this process corresponds to perform formal Gaussian elimination over

$$\left[\begin{array}{ccc|c} L_k & D_k & U_k & s^{(k)} \\ 0 & L_{k+1} & \Delta_{k+1} & \sigma^{(k+1)} \end{array} \right], \qquad (38)$$

to eliminate U_k in the first row.

(ii) **Backward substitution**

Once we have the system of equations in the form (37) it is immediate to solve recursively

$$f^{(k)} = \Delta_k^{-1} \left(\sigma^{(k)} - L_k f^{(k-1)} \right), \qquad (39)$$

for $k = 0, 1, \dots, N_\xi$ (in this order). Here, we denote by $\Delta_0^{-1} \sigma^{(0)}$ to the solution that satisfies (34). We recall that for $k = 0$, we must impose condition (34) so that $\Delta_0 f^{(0)} = \sigma^{(0)}$ has a unique solution. As $L_1 = \boldsymbol{b} \cdot \nabla$, using expression (27), it is apparent from equation (39) that the integration constant does not affect the value of $f^{(1)}$.

We can apply this algorithm to solve equation (16) for f_1, f_2 and f_3 in order to compute approximations to the transport coefficients. In terms of the Legendre modes of f_1, f_2 and f_3, the monoenergetic geometric coefficients from definition (24) read

$$\widehat{D}_{11} = 2 \left\langle s_1^{(0)} f_1^{(0)} \right\rangle + \frac{2}{5} \left\langle s_1^{(2)} f_1^{(2)} \right\rangle, \qquad (40)$$

$$\widehat{D}_{31} = \frac{2}{3} \left\langle B f_1^{(1)} \right\rangle, \qquad (41)$$

$$\widehat{D}_{13} = 2 \left\langle s_1^{(0)} f_3^{(0)} \right\rangle + \frac{2}{5} \left\langle s_1^{(2)} f_3^{(2)} \right\rangle, \qquad (42)$$

$$\widehat{D}_{33} = -\frac{2}{3} \left\langle B f_3^{(1)} \right\rangle, \qquad (43)$$

where $3s_1^{(0)}/2 = 3s_1^{(2)} = \boldsymbol{B} \times \nabla \psi \cdot \nabla B / B^3$. Note that, in order to compute the monoenergetic geometric coefficients $\widehat{D}_{ij}$ from expressions (40), (41), (42) and (43), we only need to calculate the Legendre modes $k = 0, 1, 2$ of the solution and we can stop the backward substitution (39) at $k = 2$. In the next subsection we will explain how MONKES approximately solves equation (30) using this algorithm.

3.2. Spatial discretization and algorithm implementation

The algorithm described above allows, in principle, to compute the exact solution to the truncated drift-kinetic equation (30) which is an approximate solution to (16). However, it is not possible, to our knowledge, to give an exact expression for the operator Δ_k^{-1} except for $k = N_\xi \geq 1$. Instead, we are forced to compute an approximate solution to (30). In order to obtain an approximate solution of equation (30) we assume that each $f^{(k)}$ has a finite Fourier spectrum so that it can be expressed as

$$f^{(k)}(\theta, \zeta) = \boldsymbol{I}(\theta, \zeta) \cdot \boldsymbol{f}^{(k)}, \qquad (44)$$

where the Fourier interpolant row vector map $\boldsymbol{I}(\theta, \zeta)$ is defined at Appendix C and the column vector $\boldsymbol{f}^{(k)} \in \mathbb{R}^{N_{\mathrm{fs}}}$ contains $f^{(k)}$ evaluated at the equispaced grid points

$$\theta_i = 2\pi i / N_\theta, \qquad i = 0, 1, \dots, N_\theta - 1, \quad (45)$$

$$\zeta_j = 2\pi j / (N_\zeta N_p), \qquad j = 0, 1, \dots, N_\zeta - 1. \quad (46)$$

Here, $N_{\mathrm{fs}} := N_\theta N_\zeta$ is the number of points in which we discretize the flux surface being N_θ and N_ζ respectively the number of points in which we divide θ and ζ. The exact solution to equation (30) in general has an infinite Fourier spectrum and cannot exactly be written as (44), but taking N_θ and N_ζ sufficiently big, we can approximate the solution to equation (30) to arbitrary degree of accuracy (in infinite precision arithmetic). As is explained in Appendix C, introducing the Fourier interpolant (44) in equation (30) and then evaluating the result at the grid points, we obtain a system of $N_{\mathrm{fs}} \times (N_\xi + 1)$ equations which can be solved for $\{\boldsymbol{f}^{(k)}\}_{k=0}^{N_\xi}$. This system of equations is obtained by substituting the operators L_k, D_k, U_k in equation (30) by the $N_{\mathrm{fs}} \times N_{\mathrm{fs}}$ matrices $\boldsymbol{L}_k, \boldsymbol{D}_k, \boldsymbol{U}_k$, defined in Appendix C. Thus, we discretize (30) as

$$\boldsymbol{L}_k \boldsymbol{f}^{(k-1)} + \boldsymbol{D}_k \boldsymbol{f}^{(k)} + \boldsymbol{U}_k \boldsymbol{f}^{(k+1)} = \boldsymbol{s}^{(k)}, \qquad (47)$$

for $k = 0, 1 \dots, N_\xi$. Obviously, this system has a block tridiagonal structure and the algorithm presented in subsection 3.1 can be applied to it. We just have to replace in equations (35), (36) and (39) the operators and functions by their matrix and vector analogues respectively. We will denote such matrix and vector analogues by boldface letters. The matrix approximation to the forward elimination procedure given by equations (35) and (36) reads

$$\boldsymbol{\Delta}_k = \boldsymbol{D}_k - \boldsymbol{U}_k \boldsymbol{\Delta}_{k+1}^{-1} \boldsymbol{L}_{k+1}, \qquad (48)$$

$$\boldsymbol{\sigma}^{(k)} = \boldsymbol{s}^{(k)} - \boldsymbol{U}_k \boldsymbol{\Delta}_{k+1}^{-1} \boldsymbol{\sigma}^{(k+1)}, \qquad (49)$$

for $k = N_\xi - 1, N_\xi - 2, \dots, 0$ (in this order). Thus, starting from $\boldsymbol{\Delta}_{N_\xi} = \boldsymbol{D}_{N_\xi}$ and $\boldsymbol{\sigma}^{(N_\xi)} = \boldsymbol{s}^{(N_\xi)}$ all

the matrices $\boldsymbol{\Delta}_k$ and the vectors $\boldsymbol{\sigma}^{(k)}$ are defined from equations (48) and (49). In order to obtain the matrix $\boldsymbol{\Delta}_k$ from equation (48) requires to invert $\boldsymbol{\Delta}_{k+1}$, perform two matrix multiplications and a subtraction of matrices. The inversion using LU factorization and each matrix multiplication require $O(N_{\text{fs}}^3)$ operations so it is desirable to reduce the number of matrix multiplications to one. For $k \geq 2$, we can reduce the number of matrix multiplications in determining $\boldsymbol{\Delta}_k$ to one if instead of computing $\boldsymbol{\Delta}_{k+1}^{-1}$ we solve for $\boldsymbol{X}_{k+1}$ the matrix system of equations

$$\boldsymbol{\Delta}_{k+1}\boldsymbol{X}_{k+1} = \boldsymbol{L}_{k+1}, \qquad (50)$$

and then obtain

$$\boldsymbol{\Delta}_k = \boldsymbol{D}_k - \boldsymbol{U}_k\boldsymbol{X}_{k+1}, \qquad (51)$$

for $k = N_\xi - 1, N_\xi - 2, \ldots, 2$. For $k \leq 1$ as we need to solve (37) and do the backward substitution (39), it is convenient to compute and store $\boldsymbol{\Delta}_k^{-1}$. Besides, as none of the source terms s_1, s_2 and s_3 given by (17) have Legendre modes greater than 2 we have from equation (49) that $\boldsymbol{\sigma}^{(k)} = 0$ for $k \geq 3$ and $\boldsymbol{\sigma}^{(2)} = \boldsymbol{s}^{(2)}$ and (49) must be applied just when $k = 0$ and $k = 1$. Applying once (49) requires $O(N_{\text{fs}}^2)$ operations and its contribution to the arithmetic complexity of the algorithm is subdominant with respect to the matrix inversions and multiplications. As the resolution of a matrix system of equations and matrix multiplication must be done $N_\xi + 1$ times, numerically solving equation (47) by this method requires $O(N_\xi N_{\text{fs}}^3)$ operations. In what concerns to memory resources, as we are only interested in the Legendre modes 0, 1 and 2, it is not necessary to store in memory all the matrices $\boldsymbol{L}_k$, $\boldsymbol{D}_k$, $\boldsymbol{U}_k$ and $\boldsymbol{\Delta}_k$. Instead, we store solely $\boldsymbol{L}_k$, $\boldsymbol{U}_k$ and $\boldsymbol{\Delta}_k^{-1}$ for $k = 0, 1, 2$. For the intermediate steps we just need to use some auxiliary matrices $\boldsymbol{L}$, $\boldsymbol{D}$, $\boldsymbol{U}$, $\boldsymbol{\Delta}$ and $\boldsymbol{X}$.

To summarize, the pseudocode of the implementation of the algorithm in MONKES is given in Algorithm 1. In the first loop from $k = N_\xi - 1$ to $k = 2$ we construct $\boldsymbol{L}_2$, $\boldsymbol{\Delta}_2^{-1}$ and $\boldsymbol{U}_2$ without saving any matrix from the intermediate steps nor computing any vector $\boldsymbol{\sigma}^{(k)}$. After that, in the second loop from $k = 1$ to $k = 0$, the matrices $\boldsymbol{L}_k$ and $\boldsymbol{\Delta}_k^{-1}$ are computed and saved for the posterior step of backward substitution.

Once we have solved (47) for $\boldsymbol{f}^{(0)}$, $\boldsymbol{f}^{(1)}$ and $\boldsymbol{f}^{(2)}$, the integrals of the flux surface average operation involved in the geometric coefficients (40), (41), (42) and (43), are conveniently computed using the trapezoidal rule, which for periodic analytic functions has geometric convergence [30]. In the next sections we will see that despite the cubic scaling in N_{fs} of the arithmetical complexity of the algorithm, it is possible to obtain fast and accurate calculations of the monoenergetic geometric coefficients at low

---

Algorithm 1 Block tridiagonal solution algorithm implemented in MONKES.

Forward elimination:

$\quad \boldsymbol{L} \leftarrow \boldsymbol{L}_{N_\xi}$ ▷ Starting value for $\boldsymbol{L}$

$\quad \boldsymbol{\Delta} \leftarrow \boldsymbol{D}_{N_\xi}$ ▷ Starting value for $\boldsymbol{\Delta}$

$\quad$ **for** $k = N_\xi - 1$ **to** 2 **do**

$\quad\quad$ Solve $\boldsymbol{\Delta X} = \boldsymbol{L}$ ▷ Compute $\boldsymbol{X}_{k+1}$ stored in $\boldsymbol{X}$

$\quad\quad \boldsymbol{L} \leftarrow \boldsymbol{L}_k$ ▷ Construct $\boldsymbol{L}_k$ stored in $\boldsymbol{L}$

$\quad\quad \boldsymbol{D} \leftarrow \boldsymbol{D}_k$ ▷ Construct $\boldsymbol{D}_k$ stored in $\boldsymbol{D}$

$\quad\quad \boldsymbol{U} \leftarrow \boldsymbol{U}_k$ ▷ Construct $\boldsymbol{U}_k$ stored in $\boldsymbol{U}$

$\quad\quad \boldsymbol{\Delta} \leftarrow \boldsymbol{D} - \boldsymbol{U X}$ ▷ Construct $\boldsymbol{\Delta}_k$ stored in $\boldsymbol{\Delta}$

$\quad\quad$ **if** $k = 2$ **then** ▷ Save required matrices

$\quad\quad\quad \boldsymbol{L}_k \leftarrow \boldsymbol{L}$ ▷ Save $\boldsymbol{L}_2$

$\quad\quad\quad$ Solve $\boldsymbol{\Delta}\boldsymbol{\Delta}_k^{-1} = $ Identity ▷ Compute $\boldsymbol{\Delta}_2^{-1}$

$\quad\quad\quad \boldsymbol{U}_k \leftarrow \boldsymbol{U}$ ▷ Save $\boldsymbol{U}_2$

$\quad\quad$ **end if**

$\quad$ **end for**

$\quad$ **for** $k = 1$ **to** 0 **do**

$\quad\quad$ **if** $k > 0$ $\boldsymbol{L}_k \leftarrow \boldsymbol{L}_k$ ▷ Construct and save $\boldsymbol{L}_k$

$\quad\quad \boldsymbol{D} \leftarrow \boldsymbol{D}_k$ ▷ Construct $\boldsymbol{D}_k$ stored in $\boldsymbol{D}$

$\quad\quad \boldsymbol{U}_k \leftarrow \boldsymbol{U}_k$ ▷ Construct and save $\boldsymbol{U}_k$

$\quad\quad \boldsymbol{\Delta}_k^{-1} \leftarrow \boldsymbol{D} - \boldsymbol{U}_k\boldsymbol{\Delta}_{k+1}^{-1}\boldsymbol{L}_k$ ▷ Construct $\boldsymbol{\Delta}_k$

$\quad\quad \boldsymbol{\sigma}^{(k)} \leftarrow \boldsymbol{s}^{(k)} - \boldsymbol{U}_k\boldsymbol{\Delta}_{k+1}^{-1}\boldsymbol{\sigma}^{(k+1)}$ ▷ Construct $\boldsymbol{\sigma}^{(k)}$

$\quad\quad$ Solve $\boldsymbol{\Delta}\boldsymbol{\Delta}_k^{-1} = $ Identity ▷ Compute $\boldsymbol{\Delta}_k^{-1}$

$\quad$ **end for**

Backward substitution:

$\quad \boldsymbol{f}^{(0)} \leftarrow \boldsymbol{\Delta}_0^{-1}\boldsymbol{\sigma}^{(0)}$

$\quad$ **for** $k = 1$ **to** 2 **do**

$\quad\quad \boldsymbol{f}^{(k)} \leftarrow \boldsymbol{\Delta}_k^{-1}\left(\boldsymbol{\sigma}^{(k)} - \boldsymbol{L}_k\boldsymbol{f}^{(k-1)}\right)$

$\quad$ **end for**

---

collisionality (in particular $\widehat{D}_{31}$) in a single processor. The reason behind this is that in the asymptotic relation $O(N_{\text{fs}}^3) \sim C_{\text{alg}}N_{\text{fs}}^3$, the constant C_{alg} is small enough to allow N_{fs} to take a value sufficiently high to capture accurately the spatial dependence of the distribution function without increasing much the wall-clock time. The algorithm is implemented in the new code MONKES, written in Fortran language. The matrix inversions and multiplications are computed using the linear algebra library LAPACK [31].

4. Numerical results and benchmark

In this section we will show how MONKES provides fast and accurate calculations of the monoenergetic coefficients from low ($\hat{\nu} = 10^{-5}$ m^{-1}) to high collisionality ($\hat{\nu} = 3 \cdot 10^2$ m^{-1}) benchmarked with DKES and for some cases in which DKES calculations are not accurate, also with SFINCS. The quantity $\hat{\nu}$ is called CMUL in the code DKES. The quantity $\hat{E}_\psi$ is related to the variable EFIELD from DKES as EFIELD $= \hat{E}_\psi \, \mathrm{d}\psi/\mathrm{d}r$ where $r^2/L_a^2 = \psi/\psi_{\text{lcfs}}$ and L_a is the minor radius of

the device and we denote by $\hat{E}_r := \hat{E}_\psi \, \mathrm{d}\psi/\mathrm{d}r$ to this quantity.

4.1. Convergence of monoenergetic coefficients at low collisionality

In this subsection we will demonstrate how the monoenergetic coefficients computed by MONKES converge with N_θ, N_ζ and N_ξ for three different magnetic configurations at a single flux surface. Two of them correspond to two modes of operation of of W7-X: W7-X EIM (also called standard), W7-KJM (also called high mirror). The third one corresponds to the new QI "flat mirror" configuration CIEMAT-QI [9]. The calculations are for the collisionality $\hat{\nu} = 10^{-5}$ in the $1/\nu$ ($\hat{E}_r = 0$) and $\sqrt{\nu}$ regimes. In table 1 the list of cases considered is summarized and the radial electric field values considered for the $\sqrt{\nu}$ regime in each case.

Configuration	$\psi/\psi_{\mathrm{lcfs}}$	$\hat{\nu}$ [m^{-1}]	$\hat{E}_r$ [kV · s/m^2]
CIEMAT-QI	0.250	10^{-5}	10^{-3}
W7X-EIM	0.200	10^{-5}	$3 \cdot 10^{-4}$
W7X-KJM	0.204	10^{-5}	$3 \cdot 10^{-4}$

Table 1: Cases considered to study the convergence of monoenergetic coefficients.
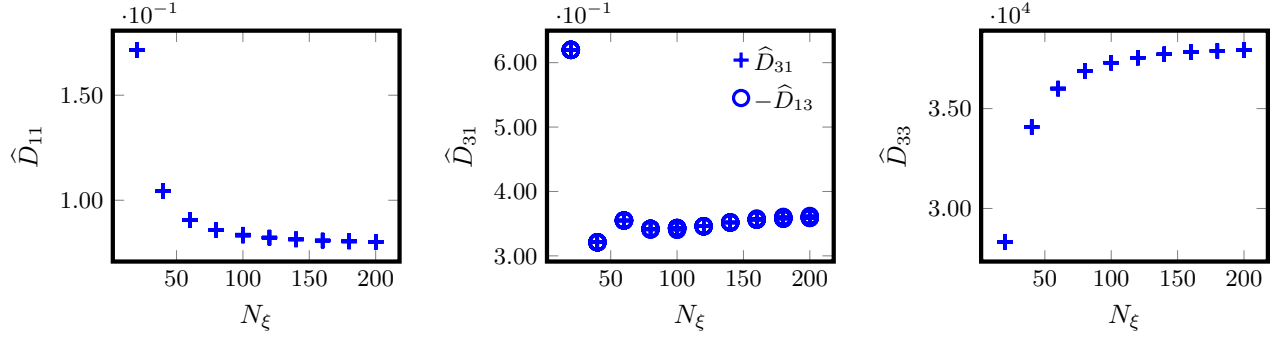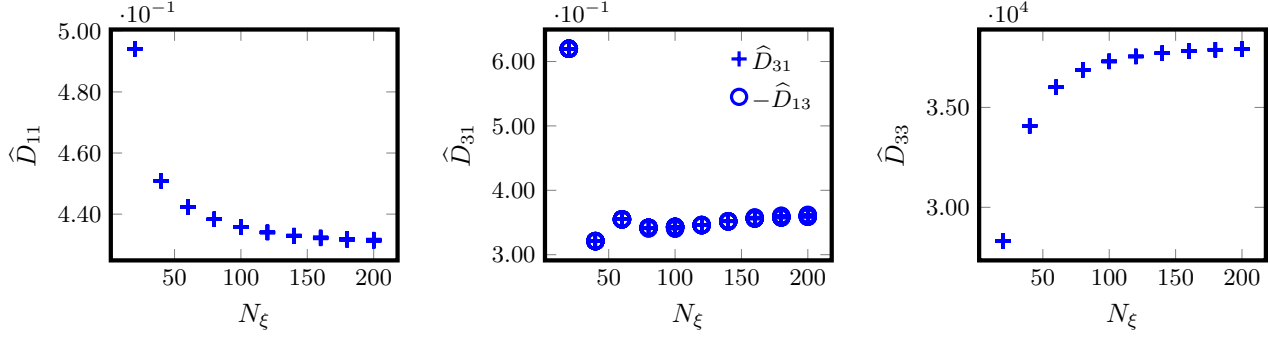
Figure 1: Convergence of monoenergetic coefficients with the number of Legendre modes N_ξ for W7X-EIM at the surface labelled by $\psi/\psi_{\text{lcfs}} = 0.200$, for $\hat{\nu}(v) = 10^{-5}$ m^{-1} and $\hat{E}_r(v) = 0$ kV $\cdot$ s/m^2.
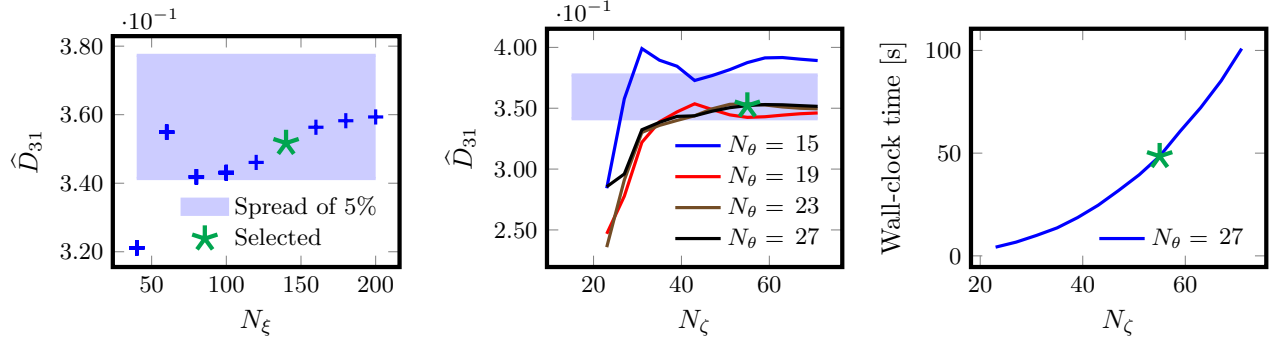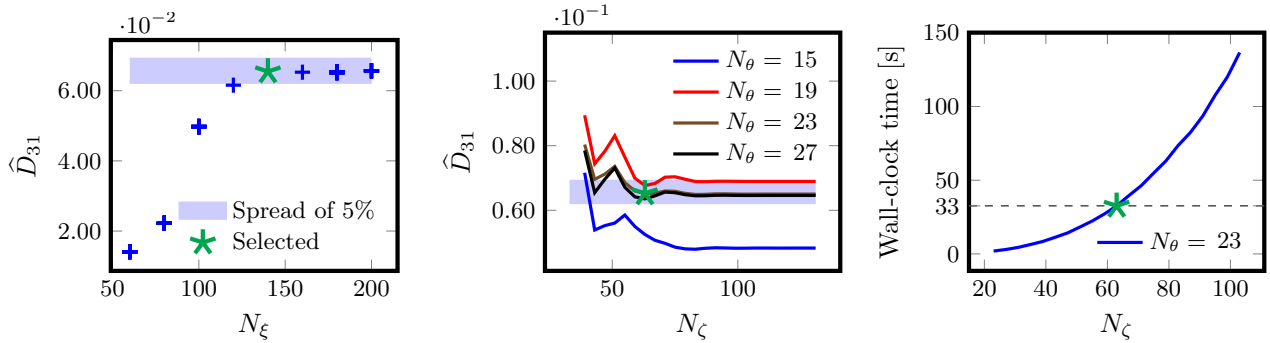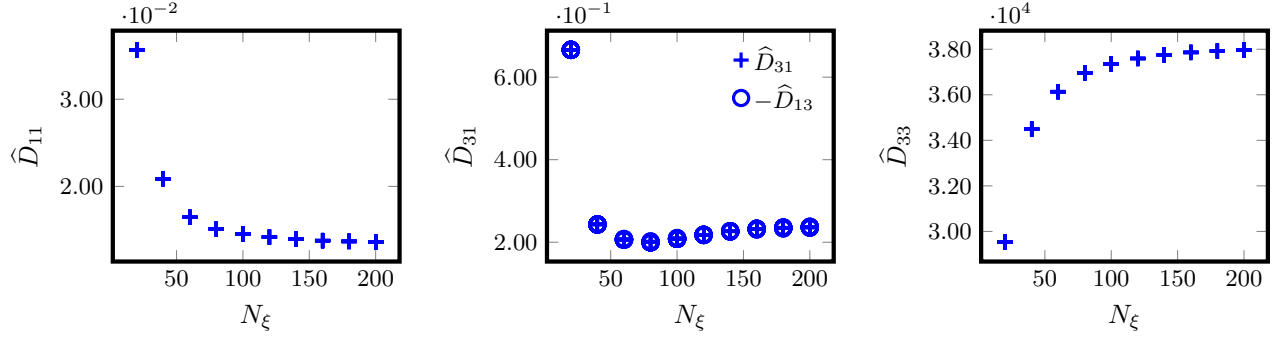

Figure 2: Selection of the resolution to have a sufficiently accurate calculation of the parallel flow geometric coefficient $\widehat{D}_{31}$ for W7X-EIM at the surface labelled by $\psi/\psi_{\text{lcfs}} = 0.200$, for $\hat{\nu}(v) = 10^{-5}$ m^{-1} and $\hat{E}_r(v) = 0$ kV $\cdot$ s/m^2. TO DO: SUBSTITUTE THE CLOCK TIME PLOT.
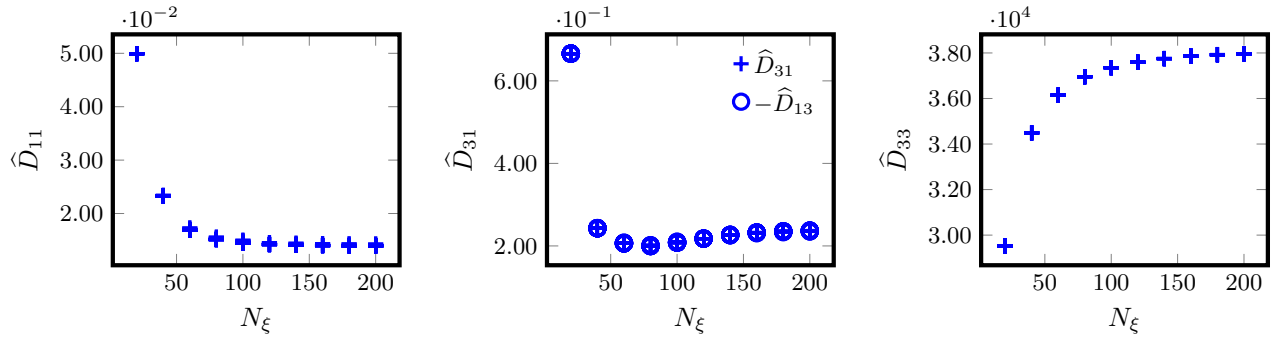
Figure 3: Convergence of monoenergetic coefficients with the number of Legendre modes N_ξ for W7X-EIM at the surface labelled by $\psi/\psi_{\text{lcfs}} = 0.200$, for $\hat{\nu}(v) = 10^{-5}$ m^{-1} and $\hat{E}_r = 3 \cdot 10^{-4}$ kV $\cdot$ s/m^2.
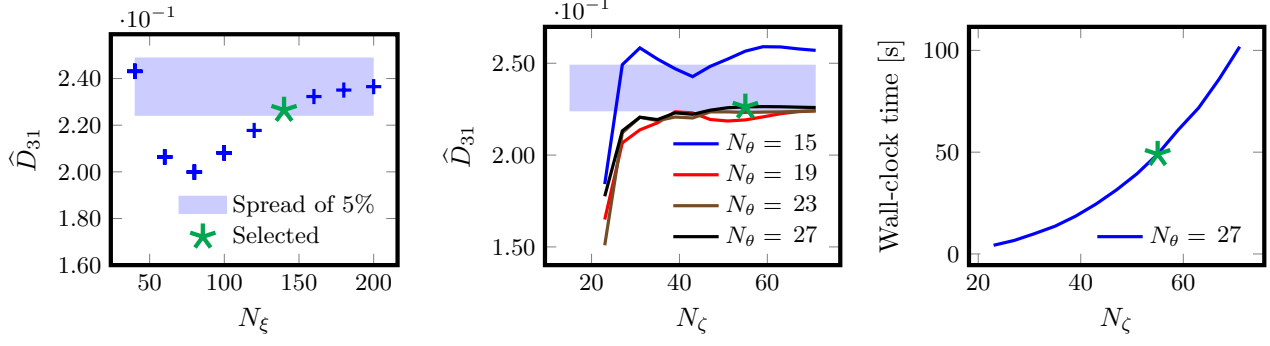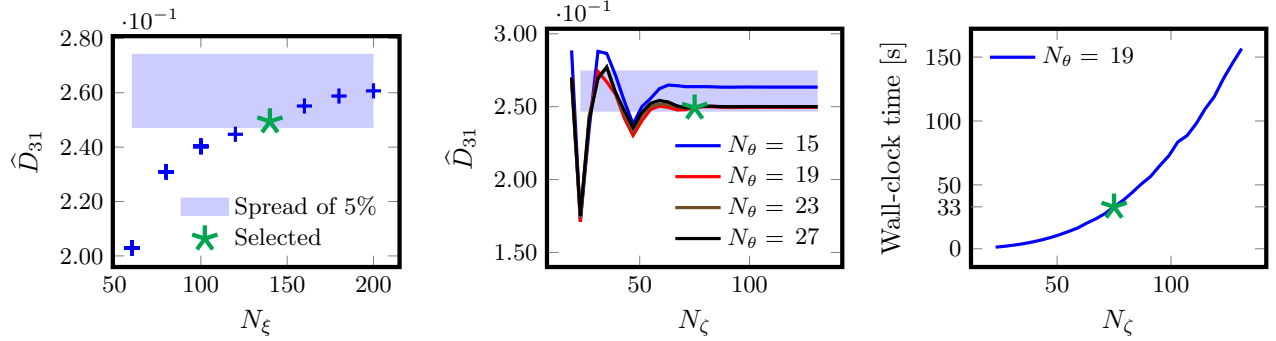
Figure 4: Selection of the resolution to have a sufficiently accurate calculation of the parallel flow geometric coefficient $\widehat{D}_{31}$ for W7X-EIM at the surface labelled by $\psi/\psi_{\mathrm{lcfs}} = 0.200$, for $\hat{\nu}(v) = 10^{-5}$ m^{-1} and $\hat{E}_r(v) = 3\cdot10^{-4}$ kV$\cdot$s/m^2. TO DO: SUBSTITUTE THE CLOCK TIME PLOT.

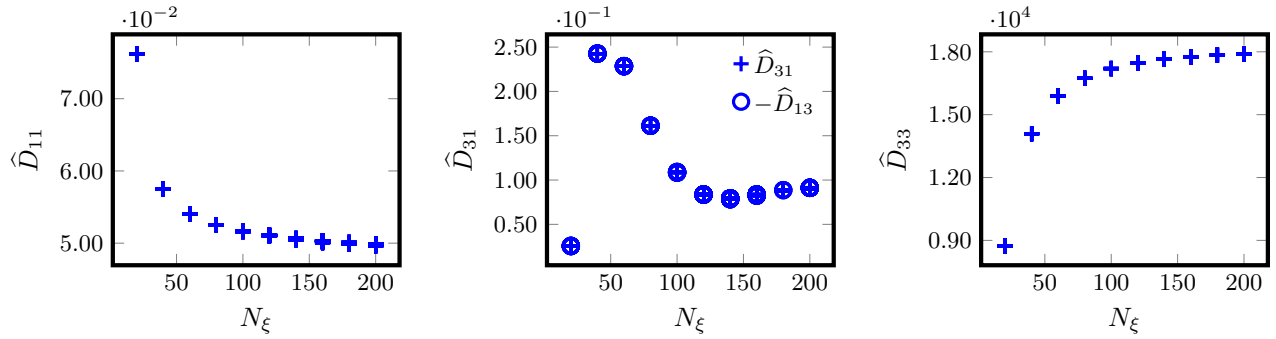

Figure 5: Convergence of monoenergetic coefficients with the number of Legendre modes N_ξ for W7X-KJM at the surface labelled by $\psi/\psi_{\mathrm{lcfs}} = 0.204$, for $\hat{\nu}(v) = 10^{-5}$ m^{-1} and $\hat{E}_r(v) = 0$ kV$\cdot$s/m^2.
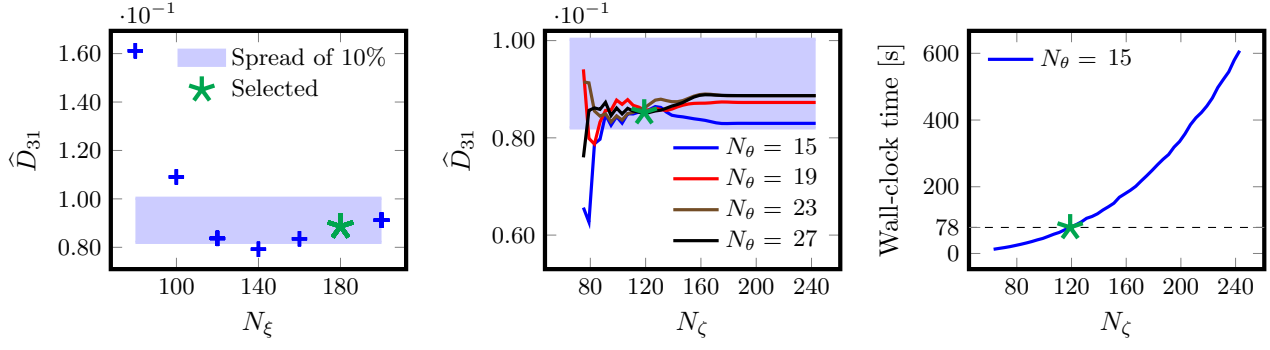

Figure 6: Selection of the resolution to have a sufficiently accurate calculation of the parallel flow geometric coefficient $\widehat{D}_{31}$ for W7X-KJM at the surface labelled by $\psi/\psi_{\mathrm{lcfs}} = 0.200$, for $\hat{\nu}(v) = 10^{-5}$ m^{-1} and $\hat{E}_r(v) = 0$ kV$\cdot$s/m^2.

Figure 7: Convergence of monoenergetic coefficients with the number of Legendre modes N_ξ for W7X-KJM at the surface labelled by $\psi/\psi_{\mathrm{lcfs}} = 0.204$, for $\hat{\nu}(v) = 10^{-5}$ m^{-1} and $\hat{E}_r(v) = 3 \cdot 10^{-4}$ kV $\cdot$ s/m^2.

Figure 8: Selection of the resolution to have a sufficiently accurate calculation of the parallel flow geometric coefficient $\widehat{D}_{31}$ for W7X-KJM at the surface labelled by $\psi/\psi_{\mathrm{lcfs}} = 0.200$, for $\hat{\nu}(v) = 10^{-5}$ m^{-1} and $\hat{E}_r(v) = 3 \cdot 10^{-4}$ kV $\cdot$ s/m^2.
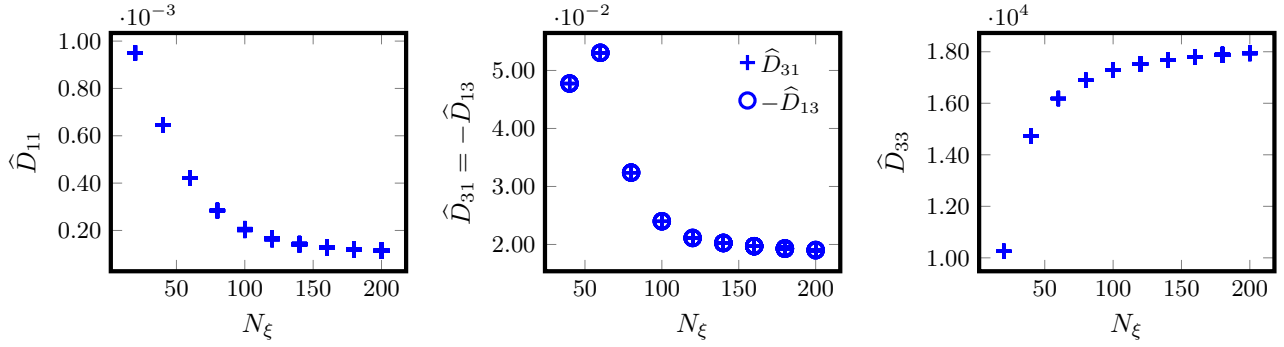

Figure 9: Convergence of monoenergetic coefficients with the number of Legendre modes N_ξ for CIEMAT-QI at the surface labelled by $\psi/\psi_{\mathrm{lcfs}} = 0.25$, for $\hat{\nu}(v) = 10^{-5}$ m^{-1} and $\hat{E}_r(v) = 0$ kV $\cdot$ s/m^2.
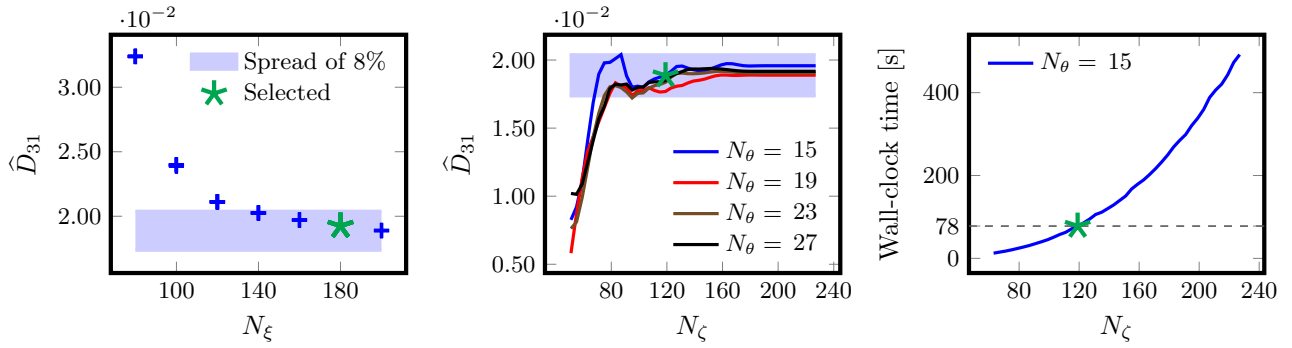
Figure 10: Selection of the resolution to have a sufficiently accurate calculation of the parallel flow geometric coefficient $\widehat{D}_{31}$ for CIEMAT-QI at the surface labelled by $\psi/\psi_{\text{lcfs}} = 0.25$, for $\hat{\nu}(v) = 10^{-5}$ m^{-1} and $\hat{E}_r(v) = 0$ kV $\cdot$ s/m^2.

Figure 11: Convergence of monoenergetic coefficients with the number of Legendre modes N_ξ for CIEMAT-QI at the surface labelled by $\psi/\psi_{\text{lcfs}} = 0.25$, for $\hat{\nu}(v) = 10^{-5}$ m^{-1} and $\hat{E}_r(v) = 10^{-3}$ kV $\cdot$ s/m^2.

Figure 12: Selection of the resolution to have a sufficiently accurate calculation of the parallel flow geometric coefficient $\widehat{D}_{31}$ for CIEMAT-QI at the surface labelled by $\psi/\psi_{\text{lcfs}} = 0.25$, for $\hat{\nu}(v) = 10^{-5}$ m^{-1} and $\hat{E}_r(v) = 10^{-3}$ kV $\cdot$ s/m^2.

4.2. Benchmark with `DKES`

(i) **Radial transport coefficient**

Configuration	ψ/ψ_{lcfs}	$\hat{\nu}$	E_r/v	$\widehat{D}_{31}$ MONKES	N_ξ	t_{clock} [s]
CIEMAT-QI	0.25	10^{-5}	0	0.07448	120	19
CIEMAT-QI	0.25	10^{-5}	10^{-3}	0.01955	140	41.95
CIEMAT-QI	0.06	10^{-5}	0	-0.007521	120	58.72
CIEMAT-QI	0.06	10^{-5}	10^{-3}	0.04413	120	14.31
W7X-KJM	0.204	10^{-5}	0	0.06523	140	31.39
W7X-KJM	0.204	10^{-5}	$3 \cdot 10^{-4}$	0.2492	140	32.22
W7X-EIM	0.200	10^{-5}	0	0.3425	140	13.95
W7X-EIM	0.200	10^{-5}	$3 \cdot 10^{-4}$	0.2262	140	35.58

Table 2: Table of MONKES results. TO DO: UPDATE D31, Nxi, TIME

Configuration	ψ/ψ_{lcfs}	$\hat{\nu}$	E_r/v	Γ_{31} DKES	Γ_{31} DKES 5%	N_ξ 5%	t_{cpu} [s] 5%
CIEMAT-QI	0.25	10^{-5}	0	0.168	0.171	100	238
CIEMAT-QI	0.25	10^{-5}	10^{-3}	0.0088	0.0086	120	214
CIEMAT-QI	0.06	10^{-5}	0	-0.048	-0.045	120	68
CIEMAT-QI	0.06	10^{-5}	10^{-3}	0.039	0.037	120	111
W7X-KJM	0.204	10^{-5}	0	0.0696	0.0692	120	615
W7X-KJM	0.204	10^{-5}	$3 \cdot 10^{-4}$	0.2693	0.2638	60	248
W7X-EIM	0.200	10^{-5}	0	0.3594	0.3705	80	83.9
W7X-EIM	0.200	10^{-5}	$3 \cdot 10^{-4}$	0.2356	0.2376	80	57.5

Table 3: Table of DKES results
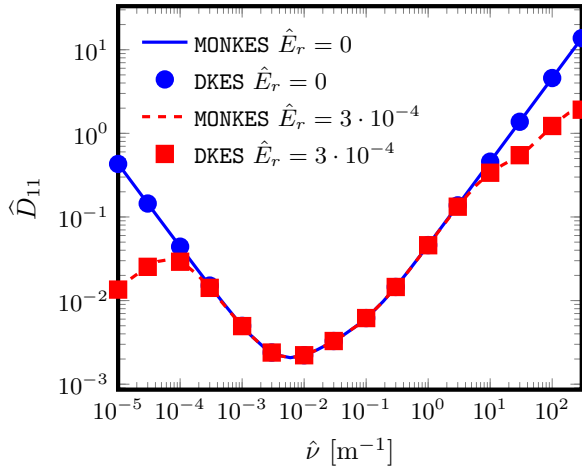
Figure 13: Calculation of $\widehat{D}_{11}$ by MONKES and DKES in the $1/\nu$ and $\sqrt{\nu}$ regimes for W7-X KJM at the surface $\psi/\psi_{\text{lcfs}} = 0.204$. $\hat{E}_r$ in kV·s/m^2.
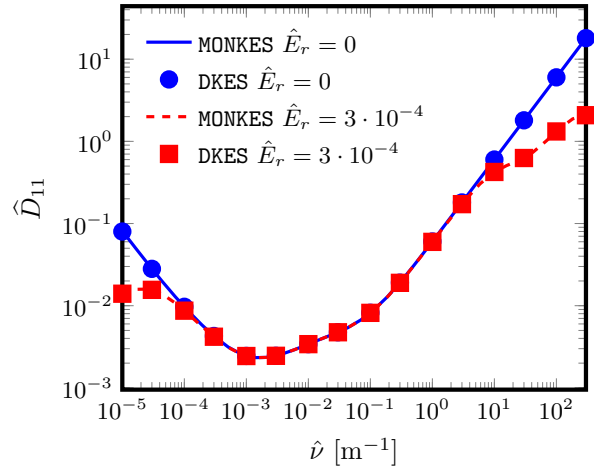
Figure 14: Calculation of $\widehat{D}_{11}$ by MONKES and DKES in the $1/\nu$ and $\sqrt{\nu}$ regimes for W7-X EIM at the surface $\psi/\psi_{\text{lcfs}} = 0.200$. $\hat{E}_r$ in kV·s/m^2.
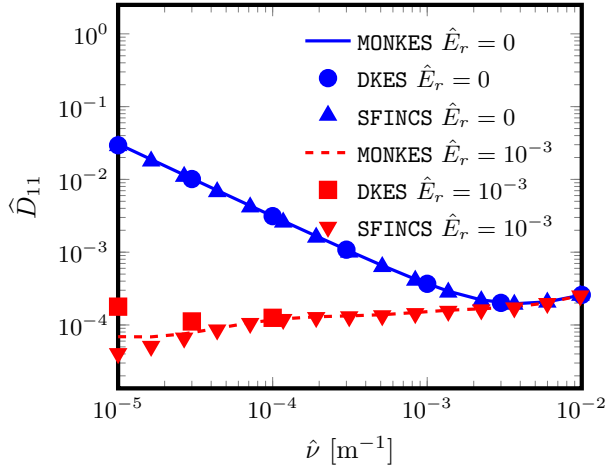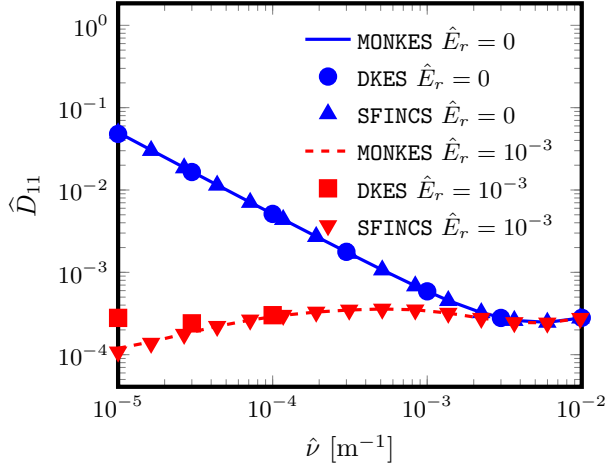
Figure 15: Calculation of $\widehat{D}_{11}$ by MONKES, DKES and SFINCS in the $1/\nu$ and $\sqrt{\nu}$ regimes for CIEMAT-QI EIM at the surface $\psi/\psi_{\text{lcfs}} = 0.060$. $\hat{E}_r$ in kV $\cdot$ s/m^2.
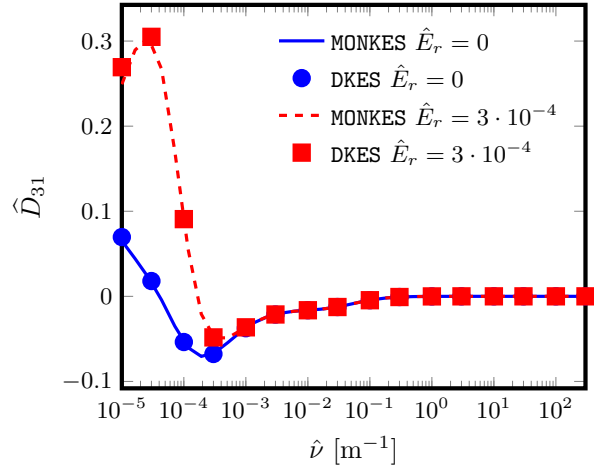

Figure 17: Calculation of $\widehat{D}_{31}$ by MONKES and DKES in the $1/\nu$ and $\sqrt{\nu}$ regimes for W7-X KJM at the surface $\psi/\psi_{\text{lcfs}} = 0.204$. $\hat{E}_r$ in kV $\cdot$ s/m^2.

Figure 16: Calculation of $\widehat{D}_{31}$ by MONKES, DKES and SFINCS in the $1/\nu$ and $\sqrt{\nu}$ regimes for CIEMAT-QI EIM at the surface $\psi/\psi_{\text{lcfs}} = 0.250$. $\hat{E}_r$ in kV $\cdot$ s/m^2.
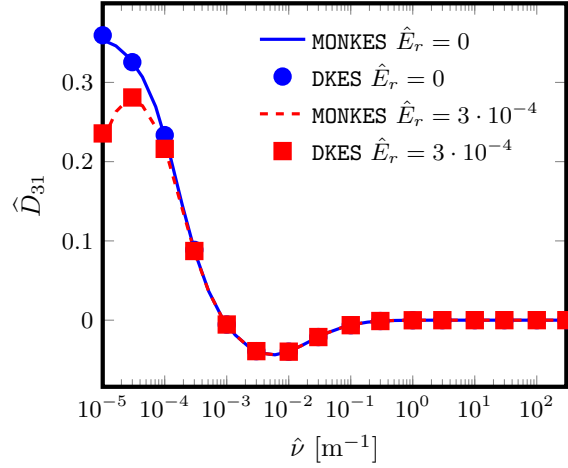

Figure 18: Calculation of $\widehat{D}_{31}$ by MONKES and DKES in the $1/\nu$ and $\sqrt{\nu}$ regimes for W7-X EIM at the surface $\psi/\psi_{\text{lcfs}} = 0.200$. $\hat{E}_r$ in kV $\cdot$ s/m^2.
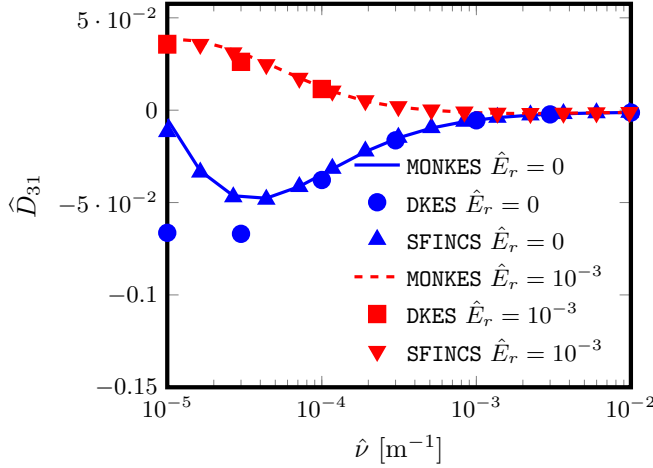
(ii) **Parallel flow coefficient**

Figure 19: Calculation of $\widehat{D}_{31}$ by `MONKES`, `DKES` and `SFINCS` in the $1/\nu$ and $\sqrt{\nu}$ regimes for CIEMAT-QI EIM at the surface $\psi/\psi_{\mathrm{lcfs}} = 0.060$. $\hat{E}_r$ in $\mathrm{kV} \cdot \mathrm{s/m}^2$.
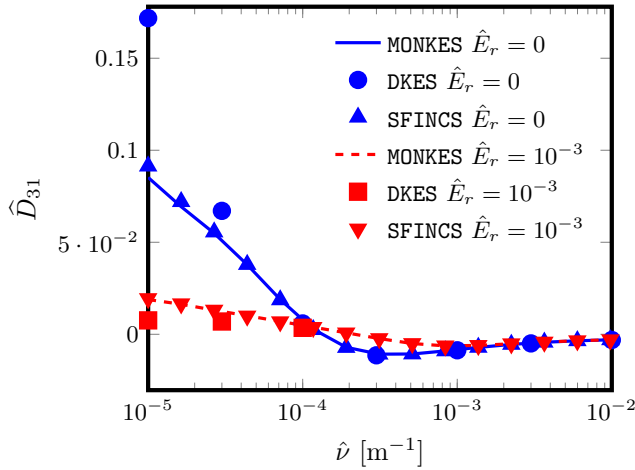

Figure 20: Calculation of $\widehat{D}_{31}$ by `MONKES`, `DKES` and `SFINCS` in the $1/\nu$ and $\sqrt{\nu}$ regimes for CIEMAT-QI EIM at the surface $\psi/\psi_{\mathrm{lcfs}} = 0.250$. $\hat{E}_r$ in $\mathrm{kV} \cdot \mathrm{s/m}^2$.

(iii) Parallel conductivity coefficient

The third and final monoenergetic coefficient is the one related to the parallel conductivity. The code `DKES` computes this coefficient measured with respect to the one obtained by solving the Spitzer problem

$$-\hat{\nu}\mathcal{L}f_{\mathrm{Sp}} = s_3, \tag{52}$$

from which using (A.1) is immediate to obtain the $1-$th Legendre mode of f_{Sp}

$$f_{\mathrm{Sp}}^{(1)} = -\frac{B}{\hat{\nu}} \tag{53}$$

and using (43) we obtain its associated $\widehat{D}_{33}$ coefficient

$$\widehat{D}_{33,\mathrm{Sp}} = -\frac{2}{3\hat{\nu}}\langle B^2 \rangle. \tag{54}$$

Figure 21: Calculation of $\widehat{D}_{33}$ by `MONKES` and `DKES` in the $1/\nu$ and $\sqrt{\nu}$ regimes for W7-X KJM at the surface $\psi/\psi_{\mathrm{lcfs}} = 0.204$. $\hat{E}_r$ in $\mathrm{kV} \cdot \mathrm{s/m}^2$.
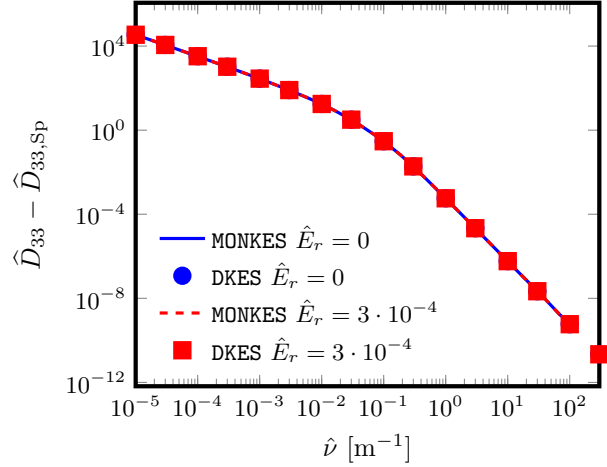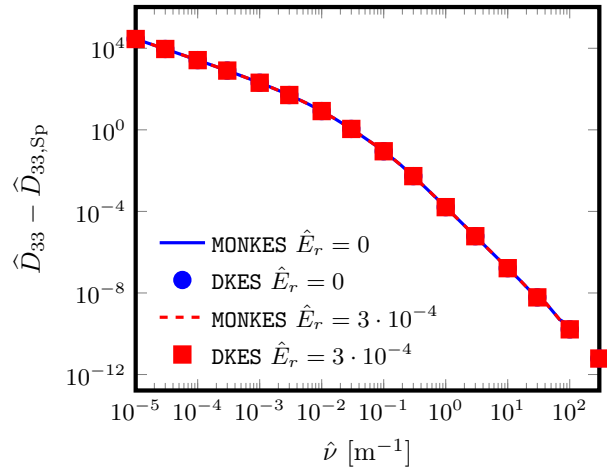

Figure 22: Calculation of $\widehat{D}_{33}$ by `MONKES` and `DKES` in the $1/\nu$ and $\sqrt{\nu}$ regimes for W7-X EIM at the surface $\psi/\psi_{\mathrm{lcfs}} = 0.200$. $\hat{E}_r$ in $\mathrm{kV} \cdot \mathrm{s/m}^2$.

5. Conclusions and future work

– PARALLELIZE MATRIX MULTIPLICATIONS AND INVERSION

– INVERSION WITH GMRES AND PRECONDITIONER BASED ON APPROXIMATING THE SCHUR COMPLEMENTS

– MOMENTUM CONSERVATION

– SOLVE ADJOINT EQUATION CAN ALSO BE DONE FAST TO APPLY ADJOINT METHODS OR COMPUTE RIGOROUS BOUNDS

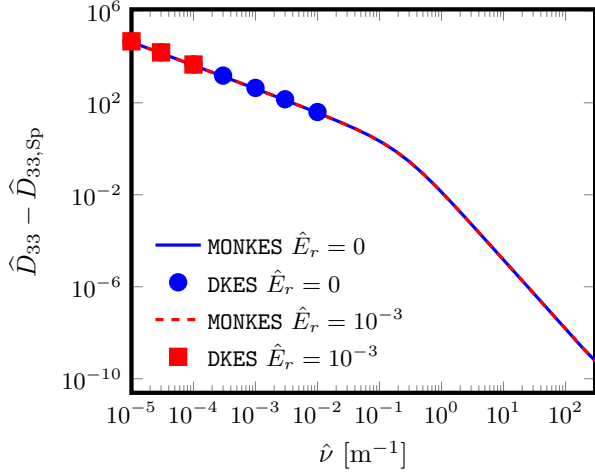– EXTENSION TO NON STELLARATOR SYMMETRIC IS IMMEDIATE

Figure 23: Calculation of $\widehat{D}_{33}$ by MONKES, DKES and SFINCS in the $1/\nu$ and $\sqrt{\nu}$ regimes for CIEMAT-QI EIM at the surface $\psi/\psi_{\text{lcfs}} = 0.250$. $\hat{E}_r$ in kV $\cdot$ s/m^2.

THIS IS JUST A PARAGRAPH CUT AND PASTED FROM OLD STUFF: An important missing feature of the pitch-angle scattering collision operator used in equation (1) is the lack of parallel momentum conservation, i.e. $\int v\xi\nu^a \mathcal{L}F_a \, \mathrm{d}^3\boldsymbol{v}$ is not identically zero. This lack of conservation introduces an spurious parallel force in the macroscopic momentum equation that can be obtained from kinetic equation (1). Hence, the parallel transport predicted by equation (1) is not correct. Fortunately, there exist techniques (see e.g. [32] or [33]) to calculate the parallel transport associated to more accurate momentum conserving collision operators by just solving the simplified drift-kinetic equation (16). This has been done successfully in the past by the code PENTA [34, 24] which uses the results of DKES to compute neoclassical transport with a more refined collision operator that preserves momentum.

Appendices

A. Legendre modes of the drift-kinetic equation

Legendre polynomials are the eigenfunctions of the Sturm-Liouville problem in the interval $\xi \in [-1, 1]$ defined by the differential equation

$$2\mathcal{L}P_k(\xi) = -k(k+1)P_k(\xi), \tag{A.1}$$

where $k \geq 0$ is an integer, and regularity boundary conditions at $\xi = \pm 1$

$$(1 - \xi^2)\frac{\mathrm{d}P_k}{\mathrm{d}\xi}\bigg|_{\xi=\pm 1} = 0. \tag{A.2}$$

As $\mathcal{L}$ has a discrete spectrum and is self-adjoint with respect to the inner product

$$\langle f, g \rangle_{\mathcal{L}} := \int_{-1}^{1} fg \, \mathrm{d}\xi, \tag{A.3}$$

in the space of functions that satisfy the regularity condition, $\{P_k\}_{k=0}^{\infty}$ is an orthogonal basis satisfying $\langle P_j, P_k \rangle_{\mathcal{L}} = 2\delta_{jk}/(2k+1)$. Hence, these polynomials satisfy the three-term recurrence formula

$$(2k+1)\xi P_k(\xi) = (k+1)P_{k+1}(\xi) + kP_{k-1}(\xi), \tag{A.4}$$

which starting from $P_0 = 1$ and $P_1 = \xi$ defines them all. Additionally, they satisfy the differential identity

$$(1-\xi^2)\frac{\mathrm{d}P_k}{\mathrm{d}\xi} = kP_{k-1}(\xi) - k\xi P_k(\xi). \tag{A.5}$$

Identities (A.4) and (A.5) are useful to represent tridiagonally the left-hand side of equation (16) when we use the expansion (29). The $k-$th Legendre mode of the term $\xi\boldsymbol{b}\cdot\nabla f$ is expressed in terms of the modes $f^{(k-1)}$ and $f^{(k+1)}$ using (A.4)

$$\langle \xi\boldsymbol{b}\cdot\nabla f, P_k \rangle_{\mathcal{L}} = \frac{2}{2k+1}\left[\frac{k}{2k-1}\boldsymbol{b}\cdot\nabla f^{(k-1)} \right. \\ \left. +\frac{k+1}{2k+3}\boldsymbol{b}\cdot\nabla f^{(k+1)}\right]. \tag{A.6}$$

Combining both (A.4) and (A.5) allows to express the $k-$th Legendre mode of the mirror term $\nabla\cdot\boldsymbol{b}((1-\xi^2)/2)\,\partial f/\partial\xi$ in terms of the modes $f^{(k-1)}$ and $f^{(k+1)}$ as

$$\left\langle \frac{1}{2}(1-\xi^2)\nabla\cdot\boldsymbol{b}\frac{\partial f}{\partial\xi}, P_k \right\rangle_{\mathcal{L}} = \tag{A.7}$$

$$\frac{\boldsymbol{b}\cdot\nabla\ln B}{2k+1}\left[\frac{k(k-1)}{2k-1}f^{(k-1)} - \frac{(k+1)(k+2)}{2k+3}f^{(k+1)}\right],$$

where we have also used $\nabla\cdot\boldsymbol{b} = -\boldsymbol{b}\cdot\nabla\ln B$. The term proportional to $\hat{E}_\psi$ is diagonal in a Legendre representation

$$\left\langle \frac{\hat{E}_\psi}{\langle B^2 \rangle}\boldsymbol{B}\times\nabla\psi\cdot\nabla f, P_k \right\rangle_{\mathcal{L}} = \tag{A.8}$$

$$\frac{2}{2k+1}\frac{\hat{E}_\psi}{\langle B^2 \rangle}\boldsymbol{B}\times\nabla\psi\cdot\nabla f^{(k)}.$$

Finally, for the collision operator used in equation (16), as Legendre polynomials are eigenfunctions of the pitch-angle scattering operator, using (A.1) we obtain the diagonal representation

$$\langle \hat{\nu}\mathcal{L}f, P_k \rangle_{\mathcal{L}} = -\hat{\nu}\frac{k(k+1)}{2k+1}f^{(k)}. \tag{A.9}$$

B. Invertibility of the spatial differential operators

In this Appendix we will study the invertibility of the left-hand-side of (30). For this, we consider L_k, D_k and U_k as operators from the space of smooth functions on the flux-surface $\mathcal{F}$ equipped with the inner product

$$\langle f, g\rangle_{\mathcal{F}} = \frac{N_p}{4\pi^2} \oint \oint fg \, d\theta \, d\zeta, \qquad (\text{B.1})$$

and the induced norm

$$\|f\|_{\mathcal{F}} := \sqrt{\langle f, f\rangle_{\mathcal{F}}}. \qquad (\text{B.2})$$

In this setting L_k, D_k and U_k are bounded operators from $\mathcal{F}$ to $\mathcal{F}$ as all the coefficients are smooth. The operators L_k and U_k given by (31) and (33) do not have a uniquely defined inverse as they have a non zero nullspace. This is a consequence of the fact that the parallel streaming operator

$$\mathcal{V}_{\parallel} = \xi \boldsymbol{b} \cdot \nabla + \nabla \cdot \boldsymbol{b} \frac{(1 - \xi^2)}{2} \frac{\partial}{\partial \xi} \qquad (\text{B.3})$$

has a nullspace consisting of functions $g((1 - \xi^2)/B)$. Note that we can study the invertibility of L_k and U_k by studying the existence of solutions to

$$\frac{dh}{dl} + A(l)h = 0, \qquad (\text{B.4})$$

which are not identically zero. Here l is the length along magnetic field lines and $A(l)$ is a smooth function over the flux surface. It is easy to check that

$$h(l) = C_h \exp\left(-\int_0^l A(l') \, dl'\right), \qquad (\text{B.5})$$

where $C_h \in \mathbb{R}$. If $C_h \neq 0$, continuity of h on the torus implies that

$$\int_0^{L_c} A(l') \, dl' = 0, \quad \text{if } \iota \in \mathbb{Q} \qquad (\text{B.6})$$

$$\lim_{l \to \infty} \int_0^l A(l') \, dl' = 0, \quad \text{if } \iota \in \mathbb{R} \backslash \mathbb{Q}, \qquad (\text{B.7})$$

where L_c is the length required for the magnetic field line to close itself in a rational surface. On the contrary, if such limit is not 0, C_h must be zero for h to be continuous. Writing the operators L_k and U_k, in the form (B.4) gives $A(l) \propto \partial \ln B / \partial l$, and as $\ln B$ is continuous, either (B.6) or (B.7) is always satisfied. Therefore, the nullspaces of L_k and U_k are not zero, which proves that L_k and U_k are not one-to-one.

Now we will prove that if $\hat{\nu} \neq 0$, all the D_k for $k \geq 1$ are invertible. For $\hat{E}_{\psi} = 0$, D_k is just a multiplication operator and is obviously invertible if $k \neq 0$. When

$\hat{E}_{\psi} \neq 0$ the proof can be done using a similar argument to the one used for L_k and U_k, as we can transform D_k to an equation superficially very similar to (B.4). First, we change from Boozer angles (ψ, θ, ζ) to a different set of magnetic coordinates $(\tilde{\psi}, \alpha, \varphi)$ using the linear transformation

$$\begin{bmatrix} \psi \\ \theta \\ \zeta \end{bmatrix} = \begin{bmatrix} 1 & 0 & 0 \\ 0 & (1 + \iota\delta)^{-1} & \iota \\ 0 & -\delta(1 + \iota\delta)^{-1} & 1 \end{bmatrix} \begin{bmatrix} \tilde{\psi} \\ \alpha \\ \varphi \end{bmatrix} \qquad (\text{B.8})$$

where $\delta = B_\theta / B_\zeta$. In these coordinates $\boldsymbol{B} = \nabla\tilde{\psi} \times \nabla\alpha = B_{\tilde{\psi}}\nabla\tilde{\psi} + B_\varphi\nabla\varphi$ and

$$\boldsymbol{B} \times \nabla\tilde{\psi} \cdot \nabla f = B^2 \frac{\partial f}{\partial \alpha}. \qquad (\text{B.9})$$

Thus, in coordinates (α, φ), the operator D_k takes the form

$$D_k = -\hat{E}_{\psi} \frac{B^2}{\langle B^2\rangle} \frac{\partial}{\partial \alpha} + \hat{\nu} \frac{k(k+1)}{2}. \qquad (\text{B.10})$$

Hence, we want to prove that

$$-\hat{E}_{\psi} \frac{B^2}{\langle B^2\rangle} \frac{\partial g}{\partial \alpha} + \hat{\nu} \frac{k(k+1)}{2} g = s(\alpha, \varphi) \qquad (\text{B.11})$$

has a unique solution for any source s. The homogeneous and particular solution to this problem are respectively

$$g_h = G(\varphi) \exp(A_k(\alpha, \varphi)), \qquad (\text{B.12})$$

$$g_p = -\frac{\langle B^2\rangle}{\hat{E}_{\psi}} \exp(A_k(\alpha, \varphi))$$

$$\times \int_0^\alpha s(\alpha', \varphi) \exp(-A_k(\alpha', \varphi)) \frac{d\alpha'}{B^2(\alpha', \varphi)} \qquad (\text{B.13})$$

where $G(\varphi)$ is an integration constant and

$$A_k(\alpha, \varphi) = \hat{\nu} \frac{k(k+1)}{2} \frac{\langle B^2\rangle}{\hat{E}_{\psi}} \int_0^\alpha \frac{d\alpha''}{B^2(\alpha'', \varphi)}. \qquad (\text{B.14})$$

Note from (B.8), that the curves of constant φ are straight lines in the (θ, ζ) plane with slope $-\delta$. This means that there are two options if we follow one of these curves: if $\delta \in \mathbb{Q}$ it closes itself or if $\delta \in \mathbb{R} \backslash \mathbb{Q}$ it densely fills the whole flux surface. Continuity of g_h over the torus implies that in order for $G(\varphi)$ to be non zero, either

$$A_k(L_\alpha, \varphi) = 0, \quad \text{if } \delta \in \mathbb{Q}, \qquad (\text{B.15})$$

$$\text{or}$$

$$\lim_{\alpha \to \infty} A_k(\alpha, \varphi) = 0, \quad \text{if } \delta \in \mathbb{R} \backslash \mathbb{Q}, \qquad (\text{B.16})$$

where $L_\alpha > 0$ is the arc-length required for the curve of constant φ to close itself. However, with the exception

of A_0 which is identically zero, A_k never annuls for $\alpha \neq 0$. This means that for $k \geq 1$, the constant of integration $G(\varphi)$ in (B.12) is 0. Hence, for $k \geq 1$, we can write the inverse of D_k as the operator

$$D_k^{-1} s = -\frac{\langle B^2 \rangle}{\hat{E}_\psi} \exp(A_k(\alpha, \varphi)) \tag{B.17}$$

$$\times \int_0^\alpha s(\alpha', \varphi) \exp(-A_k(\alpha', \varphi)) \frac{d\alpha'}{B^2(\alpha', \varphi)},$$

and is straightforward to check that $D_k D_k^{-1} s = D_k^{-1} D_k s = s$. The operator D_0 is not invertible as it is identically zero for $\hat{E}_\psi = 0$ and $g_{\rm h} = G(\varphi)$ for $\hat{E}_\psi \neq 0$.

Finally, we will study the invertibility of the operator Δ_k

$$\Delta_k = D_k - U_k \Delta_{k+1}^{-1} L_{k+1} \tag{B.18}$$

assuming that Δ_{k+1} is bounded and invertible. For this, first, we note that in the space of functions of interest (smooth periodic functions on the torus), using a Fourier basis $\{e^{i(m\theta + nN_p\zeta)}\}_{m,n\in\mathbb{Z}}$, we can approximate any function $f(\theta, \zeta) = \sum_{m,n\in\mathbb{Z}} \hat{f}_{mn} e^{i(m\theta + nN_p\zeta)} \in \mathcal{F}$ using an approximant $\tilde{f}(\theta, \zeta)$

$$\tilde{f}(\theta, \zeta) = \sum_{-N \leq m,n \leq N} \hat{f}_{mn} e^{i(m\theta + nN_p\zeta)} \tag{B.19}$$

truncating the modes with mode number greater than some positive integer N where

$$\hat{f}_{mn} = \left\langle f, e^{i(m\theta + nN_p\zeta)} \right\rangle_{\mathcal{F}} \left\| e^{i(m\theta + nN_p\zeta)} \right\|_{\mathcal{F}}^{-2} \tag{B.20}$$

are the Fourier modes of f. Thus, we approximate $\mathcal{F}$ using a finite dimensional subspace $\mathcal{F}^N \subset \mathcal{F}$ consisting on all the functions of the form given by equation (B.19).

Hence, as they are bounded operators, we can approximate D_k, U_k, Δ_{k+1} and L_{k+1} restricted to $\mathcal{F}^N$ (and therefore Δ_k) in equation (B.18) by operators D_k^N, U_k^N, Δ_{k+1}^N and L_{k+1}^N that map any $\tilde{f} \in \mathcal{F}^N$ to the projections of $D_k \tilde{f}$, $U_k \tilde{f}$, $\Delta_{k+1} \tilde{f}$ and $L_{k+1}\tilde{f}$ onto $\mathcal{F}^N$. The operators D_k^N, U_k^N, Δ_{k+1}^N and L_{k+1}^N can be exactly represented (in a Fourier basis) by square matrices of size $\dim \mathcal{F}^N$. When the operators are invertible, these matrices are invertible aswell. Doing so, we can interpret the matrix representation of Δ_k as the Schur complement of the matrix

$$M_k^N = \begin{bmatrix} D_k^N & U_k^N \\ L_{k+1}^N & \Delta_{k+1}^N \end{bmatrix}. \tag{B.21}$$

It is well known from linear algebra that the Schur complement of M_k^N is invertible when both D_k^N and Δ_{k+1}^N are (which they are). Hence, for $k \geq 1$, the matrix representation of Δ_k^N can be inverted for any N, and therefore Δ_k is invertible. For $k = 0$, it is necessary to substitute one of the rows of $[D_k^N \ U_k^N]$ by the condition (34) so that M_k^N is invertible for any N and as Δ_1^N can be inverted, also Δ_0^N constructed in this manner for any N, which implies that Δ_0 is invertible.

C. Fourier collocation method

In this appendix we describe the Fourier collocation (also called pseudospectral) method for discretizing the angles θ and ζ to obtain the matrices $\boldsymbol{L}_k$, $\boldsymbol{D}_k$ and $\boldsymbol{U}_k$. For convenience, we will use the complex numbers version of the discretization method but for the discretization matrices we will just take their real part. We assume that the solution to equation (30) is of the form

$$f^{(k)}(\theta, \zeta) = \sum_{n=-N_{\zeta 1}/2}^{N_{\zeta 2}/2-1} \sum_{m=-N_{\theta 1}/2}^{N_{\theta 2}/2-1} \tilde{f}_{mn}^{(k)} e^{i(m\theta + nN_p\zeta)} \tag{C.1}$$

where $N_{\theta 1} = N_\theta - N_\theta \mod 2$, $N_{\theta 2} = N_\theta + N_\theta \mod 2$, $N_{\zeta 1} = N_\zeta - N_\zeta \mod 2$, $N_{\zeta 2} = N_\zeta + N_\zeta \mod 2$ for some positive integers N_θ, N_ζ. The complex numbers

$$\tilde{f}_{mn}^{(k)} := \left\langle f^{(k)}, e^{i(m\theta + nN_p\zeta)} \right\rangle_{N_\theta N_\zeta} \left\| e^{i(m\theta + nN_p\zeta)} \right\|_{N_\theta N_\zeta}^{-2}, \tag{C.2}$$

are the discrete Fourier modes (also called discrete Fourier transform),

$$\langle f, g \rangle_{N_\theta N_\zeta} := \frac{1}{N_\theta N_\zeta} \sum_{j'=0}^{N_\zeta-1} \sum_{i'=0}^{N_\theta-1} f(\theta_{i'}, \zeta_{j'}) \overline{g(\theta_{i'}, \zeta_{j'})}, \tag{C.3}$$

is the discrete inner product associated to the equispaced grid points (45), (46), $\|f\|_{N_\theta N_\zeta} := \sqrt{\langle f, f \rangle_{N_\theta N_\zeta}}$ its induced norm and $\bar{z}$ denotes the complex conjugate of z. We denote by $\mathcal{F}^{N_\theta N_\zeta}$ to the finite dimensional vector space (of dimension $N_\theta N_\zeta$) comprising all the functions that can be written in the form of expansion (C.1).

The set of functions $\{e^{i(m\theta + nN_p\zeta)}\} \subset \mathcal{F}^{N_\theta N_\zeta}$ forms an orthogonal basis for $\mathcal{F}^{N_\theta N_\zeta}$ equipped with the discrete inner product (C.3). Namely,

$$\left\langle e^{i(m\theta + nN_p\zeta)}, e^{i(m'\theta + n'N_p\zeta)} \right\rangle_{N_\theta N_\zeta} \propto \delta_{mm'} \delta_{nn'} \tag{C.4}$$

for $-N_{\theta 1}/2 \leq m \leq N_{\theta 2}/2$ and $-N_{\zeta 1}/2 \leq n \leq N_{\zeta 2}/2$. Thus, for functions lying in $\mathcal{F}^{N_\theta N_\zeta}$, discrete expansions such as (C.1) coincide with their (finite) Fourier series.

The discrete Fourier modes (C.2) are chosen so that the expansion (C.1) interpolates $f^{(k)}$ at grid points. Thus, there is a vector space isomorphism between the space of discrete Fourier modes and $f^{(k)}$ evaluated at the equispaced grid.

Combining equations (C.1), (C.2) and (C.3) we can write our Fourier interpolant as

$$
\begin{aligned}
f^{(k)}(\theta,\zeta) &= \boldsymbol{I}(\theta,\zeta) \cdot \boldsymbol{f}^{(k)} \\
&= \sum_{j'=0}^{N_\zeta-1} \sum_{i'=0}^{N_\theta-1} I_{i'j'}(\theta,\zeta) f^{(k)}(\theta_{i'},\zeta_{j'}),
\end{aligned} \quad \text{(C.5)}
$$

where $\boldsymbol{f}^{(k)} \in \mathbb{R}^{N_{\text{fs}}}$ is the state vector containing $f^{(k)}(\theta_{i'},\zeta_{j'})$. The entries of the vector $\boldsymbol{I}(\theta,\zeta)$ are the functions $I_{i'j'}(\theta,\zeta)$ given by,

$$
I_{i'j'}(\theta,\zeta) = I_{i'}^\theta(\theta) I_{j'}^\zeta(\zeta), \quad \text{(C.6)}
$$

$$
I_{i'}^\theta(\theta) = \frac{1}{N_\theta} \sum_{m=-N_{\theta1}/2}^{N_{\theta2}/2-1} e^{im(\theta-\theta_{i'})}, \quad \text{(C.7)}
$$

$$
I_{j'}^\zeta(\zeta) = \frac{1}{N_\zeta} \sum_{n=-N_{\zeta1}/2}^{N_{\zeta2}/2-1} e^{N_p in(\zeta-\zeta_{j'})}. \quad \text{(C.8)}
$$

Note that the interpolant is the only function in $\mathcal{F}^{N_\theta N_\zeta}$ which interpolates the data at the grid points, as $I_{i'}^\theta(\theta_i) = \delta_{ii'}$ and $I_{j'}^\zeta(\zeta_j) = \delta_{jj'}$. Inserting the interpolant (C.5) in the left-hand side of equation (30) and evaluating the result at grid points gives

$$
\left.\left(L_k f^{(k-1)} + D_k f^{(k)} + U_k f^{(k)} \right)\right|_{(\theta_i,\zeta_j)} = \quad \text{(C.9)}
$$

$$
\left.\left(L_k \boldsymbol{I} \cdot \boldsymbol{f}^{(k-1)} + D_k \boldsymbol{I} \cdot \boldsymbol{f}^{(k)} + U_k \boldsymbol{I} \cdot \boldsymbol{f}^{(k+1)} \right)\right|_{(\theta_i,\zeta_j)}.
$$

Here, $L_k \boldsymbol{I}(\theta_i,\zeta_j)$, $D_k \boldsymbol{I}(\theta_i,\zeta_j)$ and $U_k \boldsymbol{I}(\theta_i,\zeta_j)$ are respectively the rows of $\boldsymbol{L}_k$, $\boldsymbol{D}_k$ and $\boldsymbol{U}_k$ associated to the grid point (θ_i,ζ_j). We can relate them to the actual positions they will occupy in the matrices choosing an ordenation of rows and columns. If we use the ordenation that relates respectively the row i_{r} and column i_{c} to the grid points (θ_i,ζ_j) and $(\theta_{i'},\zeta_{j'})$ as

$$
i_{\text{r}} = 1 + i + j N_\theta, \quad \text{(C.10)}
$$

$$
i_{\text{c}} = 1 + i' + j' N_\theta, \quad \text{(C.11)}
$$

for $i,i' = 0,1,\ldots,N_\theta - 1$ and $j,j' = 0,1,\ldots,N_\zeta - 1$. With this ordenation, we define the elements of the row i_{r} and column i_{c} given by (C.10) and (C.11) of the matrices $\boldsymbol{L}_k$, $\boldsymbol{D}_k$ and $\boldsymbol{U}_k$ to be

$$
(\boldsymbol{L}_k)_{i_{\text{r}} i_{\text{c}}} = L_k I_{i'j'}(\theta_i,\zeta_j), \quad \text{(C.12)}
$$

$$
(\boldsymbol{D}_k)_{i_{\text{r}} i_{\text{c}}} = D_k I_{i'j'}(\theta_i,\zeta_j), \quad \text{(C.13)}
$$

$$
(\boldsymbol{U}_k)_{i_{\text{r}} i_{\text{c}}} = U_k I_{i'j'}(\theta_i,\zeta_j). \quad \text{(C.14)}
$$

Explicitly,

$$
\begin{aligned}
\left. L_k I_{i'j'} \right|_{(\theta_i,\zeta_j)} = \frac{k}{2k-1} &\left(\boldsymbol{b}\cdot\nabla I_{i'j'} \Big|_{(\theta_i,\zeta_j)} \right. \\
&\left. + \frac{k-1}{2}\, \boldsymbol{b}\cdot\nabla\ln B \Big|_{(\theta_i,\zeta_j)} \delta_{ii'}\delta_{jj'} \right),
\end{aligned} \quad \text{(C.15)}
$$

$$
\begin{aligned}
\left. D_k I_{i'j'} \right|_{(\theta_i,\zeta_j)} = \frac{\hat{E}_\psi}{\langle B^2\rangle}\, &\boldsymbol{B}\times\nabla\psi\cdot\nabla I_{i'j'} \Big|_{(\theta_i,\zeta_j)} \\
&+ \frac{k(k+1)}{2}\hat{\nu}\delta_{ii'}\delta_{jj'},
\end{aligned} \quad \text{(C.16)}
$$

$$
\begin{aligned}
\left. U_k I_{i'j'} \right|_{(\theta_i,\zeta_j)} = \frac{k+1}{2k+3} &\left(\boldsymbol{b}\cdot\nabla I_{i'j'} \Big|_{(\theta_i,\zeta_j)} \right. \\
&\left. + \frac{k+2}{2}\, \boldsymbol{b}\cdot\nabla\ln B \Big|_{(\theta_i,\zeta_j)} \delta_{ii'}\delta_{jj'} \right),
\end{aligned} \quad \text{(C.17)}
$$

where we have used expressions (27) and (28) to write

$$
\begin{aligned}
\left. \boldsymbol{b}\cdot\nabla I_{i'j'} \right|_{(\theta_i,\zeta_j)} &= \frac{B}{B_\zeta + \iota B_\theta} \Big|_{(\theta_i,\zeta_j)} \\
&\times \left(\iota\delta_{jj'} \frac{dI_{i'}^\theta}{d\theta}\Big|_{\theta_i} - \delta_{ii'} \frac{dI_{j'}^\zeta}{d\zeta}\Big|_{\zeta_j} \right)
\end{aligned} \quad \text{(C.18)}
$$

$$
\begin{aligned}
\left. \boldsymbol{B}\times\nabla\psi\cdot\nabla I_{i'j'} \right|_{(\theta_i,\zeta_j)} &= \frac{B^2}{B_\zeta + \iota B_\theta} \Big|_{(\theta_i,\zeta_j)} \\
&\times \left(B_\zeta\delta_{jj'} \frac{dI_{i'}^\theta}{d\theta}\Big|_{\theta_i} - B_\theta\delta_{ii'} \frac{dI_{j'}^\zeta}{d\zeta}\Big|_{\zeta_j} \right)
\end{aligned} \quad \text{(C.19)}
$$

We remark in first place that, for $k = 0$, the rows of $\boldsymbol{D}_0$ and $\boldsymbol{U}_0$ associated to the grid point $(\theta_0,\zeta_0) = (0,0)$, are replaced by equation (34). Finally, each state vector $\boldsymbol{f}^{(k)}$ for the Fourier interpolants contains the images $f^{(k)}(\theta_{i'},\zeta_{j'})$ at the grid points, ordered according to (C.11).

Acknowledgements

References

[1] Per Helander. Theory of plasma confinement in non-axisymmetric magnetic fields. *Reports on Progress in Physics*, 77(8):087001, jul 2014.

[2] A. Pytte and Allen H. Boozer. Neoclassical transport in helically symmetric plasmas. *The Physics of Fluids*, 24(1):88–92, 01 1981.

[3] Allen H. Boozer. Transport and isomorphic equilibria. *The Physics of Fluids*, 26(2):496–499, 02 1983.

[4] Matt Landreman and Elizabeth Paul. Magnetic fields with precise quasisymmetry for plasma confinement. *Phys. Rev. Lett.*, 128:035001, Jan 2022.

[5] C. D. Beidler, H. M. Smith, A. Alonso, T. Andreeva, J. Baldzuhn, M. N. A. Beurskens, M. Borchardt, S. A.

Bozhenkov, K. J. Brunner, H. Damm, M. Drevlak, O. P.
Ford, G. Fuchert, J. Geiger, P. Helander, U. Hergen-
hahn, M. Hirsch, U. Höfel, Ye. O. Kazakov, R. Kleiber,
M. Krychowiak, S. Kwak, A. Langenberg, H. P. Laqua,
U. Neuner, N. A. Pablant, E. Pasch, A. Pavone,
T. S. Pedersen, K. Rahbarnia, J. Schilling, E. R.
Scott, T. Stange, J. Svensson, H. Thomsen, Y. Turkin,
F. Warmer, R. C. Wolf, D. Zhang, I. Abramovic,
S. Äkäslompolo, J. Alcusón, P. Aleynikov, K. Aleynikova,
A. Ali, G. Anda, E. Ascasibar, J. P. Bähner, S. G.
Baek, M. Balden, M. Banduch, T. Barbui, W. Behr,
A. Benndorf, C. Biedermann, W. Biel, B. Blackwell,
E. Blanco, M. Blatzheim, S. Ballinger, T. Bluhm,
D. Böckenhoff, B. Böswirth, L.-G. Böttger, V. Bor-
suk, J. Boscary, H.-S. Bosch, R. Brakel, H. Brand,
C. Brandt, T. Bräuer, H. Braune, S. Brezinsek, K.-
J. Brunner, R. Burhenn, R. Bussiahn, B. Buttenschön,
V. Bykov, J. Cai, I. Calvo, B. Cannas, A. Cappa,
A. Carls, L. Carraro, B. Carvalho, F. Castejon, A. Charl,
N. Chaudhary, D. Chauvin, F. Chernyshev, M. Cian-
ciosa, R. Citarella, G. Claps, J. Coenen, M. Cole, M. J.
Cole, F. Cordella, G. Cseh, A. Czarnecka, K. Czerski,
M. Czerwinski, G. Czymek, A. da Molin, A. da Silva,
A. de la Pena, S. Degenkolbe, C. P. Dhard, M. Di-
bon, A. Dinklage, T. Dittmar, P. Drewelow, P. Drews,
F. Durodie, E. Edlund, F. Effenberg, G. Ehrke, S. El-
geti, M. Endler, D. Ennis, H. Esteban, T. Estrada,
J. Fellinger, Y. Feng, E. Flom, H. Fernandes, W. H. Fi-
etz, W. Figacz, J. Fontdecaba, T. Fornal, H. Frerichs,
A. Freund, T. Funaba, A. Galkowski, G. Gantenbein,
Y. Gao, J. García Regaña, D. Gates, B. Geiger, V. Gian-
nella, A. Gogoleva, B. Goncalves, A. Goriaev, D. Gradic,
M. Grahl, J. Green, H. Greuner, A. Grosman, H. Grote,
M. Gruca, O. Grulke, C. Guerard, P. Hacker, X. Han,
J. H. Harris, D. Hartmann, D. Hathiramani, B. Hein,
B. Heinemann, S. Henneberg, M. Henkel, J. Hernan-
dez Sanchez, C. Hidalgo, K. P. Hollfeld, A. Hölting,
D. Höschen, M. Houry, J. Howard, X. Huang, Z. Huang,
M. Hubeny, M. Huber, H. Hunger, K. Ida, T. Ilkei, S. Illy,
B. Israeli, S. Jablonski, M. Jakubowski, J. Jelonnek,
H. Jenzsch, T. Jesche, M. Jia, P. Junghanns, J. Kac-
marczyk, J.-P. Kallmeyer, U. Kamionka, H. Kasahara,
W. Kasparek, N. Kenmochi, C. Killer, A. Kirschner,
T. Klinger, J. Knauer, M. Knaup, A. Knieps,
T. Kobarg, G. Kocsis, F. Köchl, Y. Kolesnichenko,
A. Könies, R. König, P. Kornejew, J.-P. Koschin-
sky, F. Köster, M. Krämer, R. Krampitz, A. Krämer-
Flecken, N. Krawczyk, T. Kremeyer, J. Krom, I. Ksiazek,
M. Kubkowska, G. Kühner, T. Kurki-Suonio, P. A. Kurz,
M. Landreman, P. Lang, R. Lang, S. Langish, H. Laqua,
R. Laube, S. Lazerson, C. Lechte, M. Lennartz, W. Leon-
hardt, C. Li, Y. Li, Y. Liang, C. Linsmeier, S. Liu,
J.-F. Lobsien, D. Loesser, J. Loizu Cisquella, J. Lore,
A. Lorenz, M. Losert, A. Lücke, A. Lumsdaine, V. Lut-
senko, H. Maaßberg, O. Marchuk, J. H. Matthew,
S. Marsen, M. Marushchenko, S. Masuzaki, D. Mau-
rer, M. Mayer, K. McCarthy, P. McNeely, A. Meier,
D. Mellein, B. Mendelevitch, P. Mertens, D. Mikkelsen,
A. Mishchenko, B. Missal, J. Mittelstaedt, T. Mizu-
uchi, A. Mollen, V. Moncada, T. Mönnich, T. Morisaki,
D. Moseev, S. Murakami, G. Náfrádi, M. Nagel, D. Nau-
joks, H. Neilson, R. Neu, O. Neubauer, T. Ngo, D. Nico-
lai, S. K. Nielsen, H. Niemann, T. Nishizawa, R. No-
centini, C. Nührenberg, J. Nührenberg, S. Obermayer,
G. Offermanns, K. Ogawa, J. Ölmanns, J. Ongena,
J. W. Oosterbeek, G. Orozco, M. Otte, L. Pacios Ro-
driguez, N. Panadero, N. Panadero Alvarez, D. Pa-
penfuß, S. Paqay, E. Pawelec, G. Pelka, V. Perseo,
and the W7-X Team. Demonstration of reduced neo-
classical energy transport in wendelstein 7-x. *Nature*,

596(7871):221–226, Aug 2021.

[6] P Helander and J Nührenberg. Bootstrap current and
neoclassical transport in quasi-isodynamic stellarators.
Plasma Physics and Controlled Fusion, 51(5):055004, feb
2009.

[7] P. Helander, J. Geiger, and H. Maaßberg. On the
bootstrap current in stellarators and tokamaks. *Physics
of Plasmas*, 18(9), 09 2011. 092505.

[8] H Peraza-Rodriguez, J M Reynolds-Barredo, R Sanchez,
V Tribaldos, and J Geiger. Bootstrap current
control studies in the wendelstein 7-x stellarator using
the free-plasma-boundary version of the siesta mhd
equilibrium code. *Plasma Physics and Controlled
Fusion*, 60(2):025023, jan 2018.

[9] E. Sánchez, J.L. Velasco, I. Calvo, and S. Mulas. A quasi-
isodynamic configuration with good confinement of fast
ions at low plasma beta. *Nuclear Fusion*, 63(6):066037,
may 2023.

[10] R. Jorge, G.G. Plunk, M. Drevlak, M. Landreman, J.-
F. Lobsien, K. Camacho Mata, and P. Helander. A
single-field-period quasi-isodynamic stellarator. *Journal
of Plasma Physics*, 88(5):175880504, 2022.

[11] Katia Camacho Mata, Gabriel G. Plunk, and Rogerio
Jorge. Direct construction of stellarator-symmetric
quasi-isodynamic magnetic configurations. *Journal of
Plasma Physics*, 88(5):905880503, 2022.

[12] Alan Goodman, Katia Camacho Mata, Sophia A Hen-
neberg, Rogerio Jorge, Matt Landreman, Gabriel Plunk,
Hakan Smith, Ralf Mackenbach, and Per Helander.
Constructing precisely quasi-isodynamic magnetic fields,
2022.

[13] Daniel W. Dudt, Alan G. Goodman, Rory Conlin, Dario
Panici, and Egemen Kolemen. Magnetic fields with
general omnigenity, 2023.

[14] Iván Calvo, Felix I Parra, José Luis Velasco, and J Arturo
Alonso. The effect of tangential drifts on neoclassical
transport in stellarators close to omnigeneity. *Plasma
Physics and Controlled Fusion*, 59(5):055014, mar 2017.

[15] Vincent d'Herbemont, Felix I. Parra, Iván Calvo, and
José Luis Velasco. Finite orbit width effects in large
aspect ratio stellarators. *Journal of Plasma Physics*,
88(5):905880507, 2022.

[16] J.L. Velasco, I. Calvo, F.I. Parra, and J.M. García-Regaña.
Knosos: A fast orbit-averaging neoclassical code for
stellarator geometry. *Journal of Computational Physics*,
418:109512, 2020.

[17] J.L. Velasco, I. Calvo, F.I. Parra, V. d'Herbemont, H.M.
Smith, D. Carralero, T. Estrada, and the W7-X Team.
Fast simulations for large aspect ratio stellarators
with the neoclassical code knosos. *Nuclear Fusion*,
61(11):116013, sep 2021.

[18] Viktor V. Nemov, Sergei V. Kasilov, Winfried Kernbichler,
and Martin F. Heyn. Evaluation of $1/\nu$ neoclassical
transport in stellarators. *Physics of Plasmas*, 6:4622–
4632, 1999.

[19] Samuel Lazerson, John Schmitt, Caoxiang Zhu, Joshua
Breslau, All STELLOPT Developers, and USDOE Office
of Science. Stellopt, version 2.7.5, 5 2020.

[20] K. C. Shaing and J. D. Callen. Neoclassical flows and
transport in nonaxisymmetric toroidal plasmas. *The
Physics of Fluids*, 26(11):3315–3326, 11 1983.

[21] N. Nakajima, M. Okamoto, J. Todoroki, Y. Nakamura, and
M. Wakatani. Optimization of bootstrap current in a
large helical system with L = 2, August 1988.

[22] P. Helander, F. I. Parra, and S. L. Newton. Stellarator
bootstrap current and plasma flow velocity at low colli-
sionality. *Journal of Plasma Physics*, 83(2):905830206,
2017.

[23] M. Landreman, S. Buller, and M. Drevlak. Optimization
of quasi-symmetric stellarators with self-consistent

bootstrap current and energetic particle confinement. *Physics of Plasmas*, 29(8), 08 2022. 082501.

[24] H. Sugama and S. Nishimura. How to calculate the neoclassical viscosity, diffusion, and current coefficients in general toroidal plasmas. *Physics of Plasmas*, 9(11):4637–4653, 10 2002.

[25] W. I. van Rij and S. P. Hirshman. Variational bounds for transport coefficients in three-dimensional toroidal plasmas. *Physics of Fluids B: Plasma Physics*, 1(3):563–569, 1989.

[26] M. Landreman, H. M. Smith, A. Mollén, and P. Helander. Comparison of particle trajectories and collision operators for collisional transport in nonaxisymmetric plasmas. *Physics of Plasmas*, 21(4):042503, 2014.

[27] S. P. Hirshman, K. C. Shaing, W. I. van Rij, C. O. Beasley, and E. C. Crume. Plasma transport coefficients for nonsymmetric toroidal confinement systems. *The Physics of Fluids*, 29(9):2951–2959, 1986.

[28] C.D. Beidler, K. Allmaier, M.Yu. Isaev, S.V. Kasilov, W. Kernbichler, G.O. Leitold, H. Maaßberg, D.R. Mikkelsen, S. Murakami, M. Schmidt, D.A. Spong, V. Tribaldos, and A. Wakasa. Benchmarking of the mono-energetic transport coefficients—results from the international collaboration on neoclassical transport in stellarators (icnts). *Nuclear Fusion*, 51(7):076001, jun 2011.

[29] Matt Landreman. The monoenergetic approximation in stellarator neoclassical calculations. *Plasma Physics and Controlled Fusion*, 53(8):082003, jun 2011.

[30] Lloyd N. Trefethen and J. A. C. Weideman. The exponentially convergent trapezoidal rule. *SIAM Review*, 56(3):385–458, 2014.

[31] E. Anderson, Z. Bai, C. Bischof, S. Blackford, J. Demmel, J. Dongarra, J. Du Croz, A. Greenbaum, S. Hammarling, A. McKenney, and D. Sorensen. *LAPACK Users' Guide*. Society for Industrial and Applied Mathematics, Philadelphia, PA, third edition, 1999.

[32] M. Taguchi. A method for calculating neoclassical transport coefficients with momentum conserving collision operator. *Physics of Fluids B: Plasma Physics*, 4(11):3638–3643, 11 1992.

[33] H. Maaßberg, C. D. Beidler, and Y. Turkin. Momentum correction techniques for neoclassical transport in stellarators. *Physics of Plasmas*, 16(7), 07 2009. 072504.

[34] D. A. Spong. Generation and damping of neoclassical plasma flows in stellaratorsa). *Physics of Plasmas*, 12(5), 04 2005. 056114.